MUON BOREHOLE DETECTOR DEVELOPMENT FOR USE IN FOUR-DIMENSIONAL TOMOGRAPHIC DENSITY MONITORING

by

Joshua Flygare

A thesis submitted to the faculty of
The University of Utah
in partial fulfillment of the requirements for the degree of

Master of Science

in

Nuclear Engineering

Department of Civil and Environmental Engineering

The University of Utah

May 2016

The University of Utah Graduate School

STATEMENT OF THESIS APPROVAL

The thesis of **Joshua Flygare**

has been approved by the following supervisory committee members:

Azaree T. Lintereur	, Chair	**03/08/2016** Date Approved
Luther W. McDonald IV	, Member	**03/08/2016** Date Approved
Brian James MacPherson	, Member	**03/08/2016** Date Approved

and by **Michael Ernest Barber** , Chair/Dean of

the Department/College/School of **Civil and Environmental Engineering**

and by David B. Kieda, Dean of The Graduate School.

ABSTRACT

The increase of CO_2 concentrations in the atmosphere and the correlated temperature rise has initiated research into methods of carbon sequestration. One promising possibility is to store CO_2 in subsurface reservoirs of porous rock. After injection, the monitoring of the injected CO_2 is of paramount importance because the CO_2 plume, if escaped, poses health and environmental risks. Traditionally, seismic reflection methods are the chosen method of determining changes in the reservoir density due to CO_2 injection, but this is expensive and not continuous. A potential and promising alternative is to use cosmic muon tomography to determine density changes in the reservoir over a period of time. The work I have completed was the development of a muon detector that will be capable of being deployed in boreholes and perform long-term tomography of the reservoir of interest. The detector has the required dimensions, an angular resolution of approximately 2 degrees, and is robust enough to survive the caustic nature of the fluids in boreholes, as well as temperature and pressure fluctuations.

The detector design is based on polystyrene scintillating rods arrayed in alternating layers. The layers, as arranged, can provide four-dimensional (4D) tomographic data to detect small changes in density at depths up to approximately 2 kilometers. Geant4, a Monte Carlo simulation code, was used to develop and optimize the detector design. Additionally, I developed a method of determining the muon flux at depth, including CO_2 saturation changes in subsurface reservoirs. Preliminary experiments were performed at Pacific Northwest National Laboratory.

This thesis will show the simulations I performed to determine the angular resolution and background discrimination required of the detector, the experiments to determine light transport through the polystyrene scintillating rods and fibers, and the method developed to predict muon flux changes at depth expected after injection.

TABLE OF CONTENTS

ACKNOWLEDGEMENTS

I would like to thank my advisor Azaree Lintereur for her constant help and mentoring through my degree. I had the opportunity to work on an impactful and fun research project because of her connection with the Pacific Northwest National Laboratory. I would like to thank Dr. Kouzes, Dr. Bonneville, and Dr. Yamaoka for their knowledge and insights while working at PNNL. I would also like to thank my family, particularly my mom and my brother, for their encouragement and support.

CHAPTER 1

INTRODUCTION

The increase of atmospheric carbon dioxide (CO_2) concentration correlated to global temperature rise (IPPC Panel, 2014) has fueled research efforts to reduce atmospheric CO_2 emissions. Tangible risks of global temperature rise are documented extensively (IPPC Panel, 2014), suggesting that relatively simple approaches such as CO_2 capture and sequestration (CCS) of point source emissions may be justifiable. Minimizing CO_2 emissions requires either reduced production or increased sequestration. Carbon sequestration is likely only one of many emission reduction tools needed, because worldwide outputs are estimated to exceed 10 billion metric tons annually (Boden et al., 2015). One potential CCS strategy is subsurface injection into underground porous reservoirs. Carbon storage is already a byproduct of CO_2 "enhanced oil recovery" (EOR), but such storage is offset by emissions associated with the combustion of produced fuels (Faltinson et al., 2011). Prime storage reservoirs lie beneath "seal layers," low permeability formations that are demonstrated to trap oil and natural gas effectively.

In the United States, 37% of CO_2 emissions are from generation of electricity (U.S. Environmental Protection Agency, 2015), and approximately 39% of these emissions are from coal power plants. Though not the only type of plant to release CO_2, most coal has a higher carbon content than other types of fossil fuel. The U.S. has approximately 572 coal power plants which account for approximately 77% of all CO_2 output from electricity generation (as recorded in 2013), or 1575 million megatons (U.S. Environmental Protection Agency, 2015).

Existing plants may be retrofitted for carbon capture via chemical separation, cryogenic cooling or other means. The CO_2, once separated, can be pressurized to both match injection reservoir pressure and maximize CO_2 density (to maximize the amount stored).. High density CO_2 is either supercritical or liquid in phase, dictated by reservoir pressure and temperature.

Generally, the CO_2 exists as gas at depths of 700 m and less, liquid between 700 and 900 m, and supercritical at depths greater than 900 m. According to current data, the majority of effective candidate storage reservoirs lie at supercritical depths.

A critical aspect of subsurface CO_2 storage is postinjection monitoring, a requirement of the U.S. Environmental Protection Agency and its Underground Injection Control (UIC) program. The purpose of required monitoring is to minimize risks associated with leakage and other possible environmental impacts; CO_2 leakage would defeat the purpose of sequestration. Many methods of monitoring rely on detection of CO_2 density changes in layers adjacent to the storage reservoir.

One known method for such density-detection monitoring is time-lapse gravity measurements, which rely on measuring changes in the Earth's gravitational field over time. Time-lapse gravity is a well-known technique used for over 50 years. Developments in gravimeter technology (Goodkind, 1999) as well as advancements in GPS systems have led to vast improvements in the technology. However, this method can provide only discrete values of gravitational field anomalies, and is by definition an underdetermined problem. A possible solution for reservoir monitoring is cosmic ray tomography, which can provide detailed stratigraphic images. Cosmic ray tomography is also a well-known technique but only recently has provided quality images of subsurface rock formations (Tanaka et al., 2001, 2007). This cosmic ray tomography application relies on the detection of muons generated in the upper atmosphere during Extensive Air Showers (EAS). When an EAS occurs, it sends a spectrum of muons generated at various angles and energies towards the earth. Muons interact with the Earth's surface, depositing energy in a predictable way primarily through ionization and bremsstrahlung. The energy deposited by the muon can be used to track where it came from. Thus, the detector, using the predictable energy deposit, will be used to track the muon's angle of approach as well as the total flux over time.

The muons deposit energy as they pass through the 1 to 2 km of overburden and reach the detector. The number of muons that are able to reach the detector are dependent on their energy. Higher energy muons will reach the detector more frequently than low energy muons. If

the overburden above the detector were to increase, for example, from a decrease in CO_2 saturation, the number of muons with sufficient energy to pass through the additional matter would decrease, thus decreasing the overall flux. Alternatively, if the overburden were to decrease, the muon flux would increase. This increase or decrease in flux will be detected at particular angles as a decrease of muons coming from that particular angle. The larger the muon angle from vertical, the larger the overburden in that muon's path to the detector. If the number of incoming muons coming from angle Y decreases, it can be assumed that there has been a density increase in that direction. As the flux changes, or the flux from a particular angle changes, the detector will be able to resolve the approximate location of the change in overburden. Thus, for the application of CO_2 sequestration, the muon detector will ideally be able to monitor shifts in the CO_2 plume in the reservoir using changes in the angular flux.

The sensitivity required for the muon detectors used for CO_2 sequestration monitoring must be quantified and is based on two main considerations. First, what is the total flux at the depth of interest? And second, what is the angular resolution required by the detector? While physical measurements are the best way to determine the requirements they are not always practical, in which case simulations can provide insight into the necessary performance.

The total flux at the depth of interest is important because the number of muons that reach the detector will determine the statistical certainty of any measurements. It will also determine the amount of time required to make a measurement with a specific uncertainty. An empirical equation has been developed (Mei and Hime, 2006) to predict the total flux at a range of subsurface depths. A method for predicting the flux changes at various depths due to changes in rock formation density has been produced in this work, and will be discussed in Chapter 2. The second detector parameter of interest, the angular resolution, will determine its ability to effectively "bin" the incoming muons into various angles. The better the resolution, the more sensitive the binning can be, which will enable the detector to identify changes in the angular flux quicker than would be possible with poor resolution. Additionally, a detector with high resolution will more accurately predict locations where the change occurred. The exact resolution needed

will be unknown until after a detector deployment is possible. However, simulations indicate that a high resolution (< 5 degrees) will be necessary.

The detector was designed to be deployed in a standard borehole with an approximate diameter of 20 cm. The detector must fit inside of a thick pipe capable of protecting it from pressure, corrosion, and subterranean background. Once deployed, it must be capable of remaining in the borehole for decades while the reservoir is monitored.

In this thesis, a detector capable of meeting the performance capabilities required for borehole deployment has been designed using advanced simulations and preliminary experiments. The detector has a mean angular resolution of approximately two degrees, while remaining small enough for a 20 cm diameter borehole. It has an approximate area of 1050 cm^2 and is based on scintillating rods in alternating layers, providing a coordinate system for angular determination.

References

Boden, T. A.; Marland, G.; Andres, R. J. *Global, Regional, and National Fossil-Fuel CO2 Emissions.*; Oak Ridge, 2015.

Faltinson, J.; Innovates, A.; Futures, T.; Gunter, B.; Incorporated, G. B. E. Net CO2 Stored in North American EOR Projects. *J. Can. Pet. Technol.* **2011**, August, 55–60.

Goodkind, J. M. The Superconducting Gravimeter. *Rev. Sci. Instrum.* **1999**, *70* (11), 4131–4152.

IPPC Panel. *Climate Change 2014: Synthesis Report*; 2014.

Mei, D. M.; Hime, A. Muon-Induced Background Study for Underground Laboratories. *Phys. Rev. D - Part. Fields, Gravit. Cosmol.* **2006**, *73* (December 2005), 1–18.

Tanaka, H. K. M.; Nakano, T.; Takahashi, S.; Yoshida, J.; Takeo, M.; Oikawa, J.; Ohminato, T.; Aoki, Y.; Koyama, E.; Tsuji, H.; et al. High Resolution Imaging in the Inhomogeneous Crust with Cosmic-Ray Muon Radiography: The Density Structure below the Volcanic Crater Floor of Mt. Asama, Japan. *Earth Planet. Sci. Lett.* **2007**, *263* (1-2), 104–113.

Tanaka, H.; Nagamine, K.; Kawamura, N.; Nakamura, S. N.; Ishida, K.; Shimomura, K. Development of the Cosmic-Ray Muon Detection System for Probing Internal-Structure of a Volcano. In *Hyperfine Interactions*; 2001; Vol. 138, pp 521–526.

U.S. Environmental Protection Agency. *Inventory of U.S. Greenhouse Gas Emissions and Sinks: 1990 - 2013*; Washington D.C., 2015.

CHAPTER 2

MUONS AND THEIR INTERACTIONS

Muons (μ) are leptons, which are one of three categories of elementary constituents of matter, the others being quarks and gauge bosons. Muons have an electric charge of -1 e (electron charge, being 1.602×10^{-19} Coulombs) and weigh 105.7 MeV/c^2, approximately 207 times more than an electron (0.511 MeV/c^2). Muons have a spin of one-half, and as a result are classified as leptons. Additionally, they have a long lifetime compared to other free particles. Muons have a lifetime of approximately 2.2 μs, which is second only to the neutron, with a lifetime of 14.7 min. Typically, high energy particles generated in cosmic or accelerator events last on the order of only 10^{-17} to 10^{-30} s, because their decay is mediated by the strong force (Griffiths, 1987). Muons and neutrons decay through a weak force interaction, making their lifetime longer than any strong force mediated decay. Muons have high applicability in radiation detection, as the majority of cosmic background at the surface of the earth is muons (Olive et al., 2014). Muons are generated at extremely high energies. Their parent particles are usually protons or heavier hadrons generated in cosmic events such as solar flares or supernovae (Cullerne, 2009), and their energy can be unbelievably high, up to and even exceeding approximately 10^{20} eV (Drury, 2012). Additionally, due to their very high average energy at production (~ 6 GeV) (Olive et al., 2014), muons can penetrate deep into the earth before decaying or being attenuated. Thus, they are of interest in both subterranean and atmospheric experiments. The production of muons and their interactions are well-studied aspects of particle physics.

Muon Production and Decay

High-energy cosmic events, such as distant supernovae or more local solar flares, eject energetic particles into space. Generally these particles are protons, alpha particles, and heavier

nuclei, which decrease in abundance as their atomic number increases (Rebef and Sima, 2008). As these particles approach Earth they interact with its geomagnetic field and independently undergo nuclear collisions, mainly with nitrogen and oxygen nuclei. These collisions are high-energy hadronic interactions (hadrons are particles made of quarks and/or anti-quarks) that result in the production of secondary particles, such as pions (π) and kaons (K). The production of pions and kaons from the collision of a proton (p) and a nucleus (A) occurs as follows:

$$p + A \rightarrow p + X + \pi^{\pm,0} + K^{\pm,0} + \cdots$$

where X is the fragmented nucleus.

The production energy threshold of pions and kaons from this reaction can be found through a center of mass frame of reference analysis. This reveals minimum proton threshold energies of 1.08 GeV and 1.43 GeV for the pion and kaon, respectively. Free particles, such as the pions and kaons, will decay according to the forces they are subject to. The three fundamental forces that facilitate particle decay are the strong force, the weak force, and the electromagnetic force. Charged pions and kaons decay through the following mechanisms:

$$\pi^{\pm} \rightarrow \mu^{\pm} + \nu_{\mu}(\bar{\nu}_{\mu})\ 100.0\%$$
$$K^{\pm} \rightarrow \mu^{\pm} + \nu_{\mu}(\bar{\nu}_{\mu})\ 63.5\%$$
$$K^{\pm} \rightarrow \pi^{\pm} + \pi^{0}\ 36.4\%$$

where the first two are through the weak force and the last is through the strong force. The neutral pions and kaons decay as follows:

$$\pi^{0} \rightarrow \gamma + \gamma$$
$$K^{0} \rightarrow \pi^{+} + \pi^{-}$$
$$K^{0} \rightarrow \pi^{0} + \pi^{0}$$
$$K^{0} \rightarrow \pi^{\pm} + e^{\pm} + \nu_{e}(\bar{\nu}_{e})$$

Except for the neutral pion, which decays in 10^{-17} s, all of the other mentioned pion and kaon decay mechanisms have decay times around 10^{-8} to 10^{-13} s, and are controlled by the weak force. The neutral pion decay is controlled through the electromagnetic force. These particles are part of what is referred to as an extensive air shower (EAS). An EAS is a result of the primary charged particles from space causing a cascade of collisions, particle productions, and subsequent decay processes. Many of these decay schemes have a pathway to muon

production. Because a muon is a lepton, it does not experience the strong force, and hence must decay by either electromagnetic or weak interactions. The decay of the muon occurs as follows:

$$\mu^- \rightarrow e^- + \bar{\nu}_e + \nu_\mu$$
$$\mu^+ \rightarrow e^+ + \nu_e + \bar{\nu}_\mu$$

both of which occur through the weak force.

One may expect the presence of μ^- and μ^+ to be equal at the surface of the earth. However, it has been discovered that the ratio of μ^+/μ^- is closer to 1.25, the unequal distribution occurs for a few reasons, as has been stated by Gaisser (Gaisser, 2012). As seen from the previous decay schemes for pions and kaons, charge is always conserved. Consequently if the ratio of μ^+/μ^- is greater than unity, there must be greater production of positively charged mesons. This has been demonstrated (Gaisser, 2012), and is partly due to a greater number of protons than neutrons as primary cosmic particles, and from large production cross sections of positive pions and kaons. In particular, the reaction $p \rightarrow K^+$ has a larger cross section, and thus a larger contribution than its negative counterpart, or from $p \rightarrow \pi^+$. The Muon charge ratio is also a function of muon energy (Gaisser, 2012). The charge ratio increases with energy, largely due to the increasing contribution of $p \rightarrow K^+$, whereas at lower energies the ratio is smaller because $p \rightarrow \pi^+$ is not as asymmetric.

Relativistic Effects

Muons are a common example in relativistic mechanics because without the effects of space contraction and time dilation they would have no interaction with the Earth's surface. Muons are dependent on space-time effects in order to make it to earth within their 2.2 μs lifetime. The relativistic effects can be thought of in two ways: 1) from the reference frame of the muon, the Earth is moving toward the muon at such speeds that space is significantly contracted and; 2) from the reference frame of an observer on Earth, the muon experiences time dilation, where the time of the muon runs much slower than the observer on earth. For the average muon produced at approximately 6 GeV (0.99984 c) at approximately 15000 m above the earth, it would take approximately 50 μs to reach the earth, or about 20 times the lifetime of the muon. But when space-time effects are taken into account, the time experienced by the muon from the earth

observer is only 0.88 μs, and the distance seen by the muon to the earth is only 264 m. These effects, while really the same effect, are sufficient to allow the muon to reach the Earth before it decays.

Muon Spectra

The production of muons results in both an energy and angular spectrum. The energy spectrum at sea level as produced by a cosmic-ray shower generator (CRY) (Hagmann et al., 2007) simulation is shown in Figure 2.1. The muon spectrum (Berghaus for the IceCube Collaboration, 2009) is approximately exponential, with very high energies (greater than 1 TeV) occurring infrequently. The very high-energy muons are infrequent due to a lower probability of cosmic particles occurring at that energy. As the cosmic particles bombard atmospheric nuclei, they produce secondary particles, the energy of which is limited by conservation of energy requirements. Additionally, the distribution of the resulting particle energies is low at both very high and very low energies. As in chemical reaction kinetics, very few particles leave a collision with the vast majority of the energy, or with close to none. The average energy of muons at sea level is approximately 4 GeV.

The muon angular spectra at sea level is shown in Figure 2.2. It follows approximately a $\cos^2$ distribution. This shape is indicative of the physics in the initial collision that produces the muon. Greater momentum transfer happens at smaller angles, and less momentum transfer at larger angles. The majority of muons produced at large angles normal to the earth's surface do not make it before they decay. This is due to two factors: first, at larger angles the muons have further to travel before reaching the surface, and are therefore more likely to decay in the process, and second; the muons generated at large angles generally have less energy because of conservation of momentum in the initial collision, and thus receive less of a relativistic advantage.

Muon-matter Interactions

The interactions of high-energy particles with matter are important in many fields, including medicine, accelerator physics, and radiation detection. Muons are charged particles, and are quite massive, about 207 times that of an electron. Thus, as discussed in the introduction

to muons, it will be important to understand the interactions of muons with matter over a wide range of energies. This section will detail the types of interactions that muons undergo, and their respective energy ranges.

Bremsstrahlung

Bremsstrahlung is the process of energy loss caused by a deceleration when the incident particle is in close proximity to a nucleus (Bethe and Heitler, 1934). The stronger the columbic field the more likely it is to induce deceleration, followed by the energy lost being emitted as a gamma ray. Bremsstrahlung essentially converts particle energy into a gamma ray. This is a common interaction with electrons, across a wide energy range. For heavier particles, such as muons, protons, alpha particles, and nuclear fragments, it usually happens at higher energies. In fact, at high enough energies, radiative processes (one of which is bremsstrahlung) overcome the energy loss from ionization. Figure 2.3 shows the basic process of muon bremsstrahlung. The cross section for the bremsstrahlung process must account for many physical phenomena, such as the nucleus size, shape, confounding variables such as the columbic field of the orbital electrons, and others (Andreev and Bugaev, 1997).

Ionization

Ionization is the process of energy loss as a result of the primary particle directly causing an ionization by “hitting” an electron. The electron is subsequently freed from the nucleus and accelerates away. The energy loss from this event can be determined by the well-known Bethe-Bloch equation (Nakamura et al., 2010). Figure 2.4 illustrates the basic process of ionization.

Other Processes

Energy loss processes which are not as frequent (especially at the typical energies concerning this detector design), include lepton trident reactions (Macluc et al., 2006), and photonuclear interactions (Bugaev and Shlepin, 2003). Trident reactions are the production of a lepton and anti-lepton pair at very high energies from a single lepton. Photonuclear interactions are inelastic direct collisions with nuclei.

Figure 2.5 shows the energy loss contributions of bremsstrahlung and ionization processes as a function of incoming muon energy. The energy at which the radiative processes (bremsstrahlung) are larger than ionization is referred to as the critical energy. For the majority of cosmic detections, ionization events outweigh bremsstrahlung.

Muon Flux at Depth

To guide the design and optimization of the detector, and determine the accuracy required, it is important to know the muon flux at reservoir depths, and how changes in CO_2 saturation will affect that flux. Two methods to predict the flux at subsurface depths were pursued.

Method 1

The first flux prediction method starts with Equation 1, a semiempirical equation from the Particle Physics Booklet (Olive et al., 2014).

$$\frac{dN_\mu}{dE_\mu d\Omega} = \frac{0.14E_\mu^{-2.7}}{cm^2\ s\ sr\ GeV}\left(\frac{1}{1+\frac{1.1E_\mu cos\theta}{115GeV}}+\frac{0.054}{1+\frac{1.1E_\mu cos\theta}{850GeV}}\right) \quad (1)$$

Where dN_μ is the differential change in muon flux, E_μ is the energy of the muon, and Ω is the solid angle. Equation 1 is used to determine the angular and energy dependent flux at the Earth's surface. To determine the flux below the surface of the Earth this method uses Equation 1 and "projects" it to determine the underground flux by correlating muon energy with penetration depth. First, by integrating over the zenith angle from 0 (vertical) to 90 degrees, the equation becomes only a function of E_μ. Originally, the equation was only integrated from 0 to 70 degrees, where the function is most accurate. It is less accurate at greater angles because it is semi-empirical, and was optimized for the majority of muons, which come at steeper angles. Also, neglecting the very large angles makes a minimal difference in total flux numbers, changing this method in a negligible way. The flux at depth is known to closely follow a secant function, making the flux at very large angles essentially zero. The integration results in a secant function, but will not be shown here due to the analytical complexity; the actual integration was only done numerically.

Next, the muon energy was related to penetration depth, so the energy required to reach a particular depth could be used in the integration. To perform the energy integration of Equation 1, the bounds of integration had to be determined. Since the flux at depth will be dependent on the number of muons with sufficient energy to penetrate to that depth, the lower bound of integration was set to be the minimum energy required to reach the depth of interest. The upper bound was set to an arbitrarily high value (100 TeV). A function that describes the minimum energy required to reach a particular depth was derived by starting with

$$-\frac{dE_\mu}{dX} = a(E_\mu) + b(E_\mu)E_\mu \tag{2}$$

where a and b are functions of material and muon energy, which are also given in the Particle Physics Booklet on page 263 (Olive et al., 2014). If this equation were integrated with respect to dX it would give an equation for the total energy loss over a particular path. It would, however, remain a function of the constant density of the material, and would thus be an over-simplification of the nonconstant density of the overburden (rock formations) above the detector. Thus, the energy loss equation needed must be a function of the water equivalent depth of the reservoir, which accounts for the density changes and the physical depth. The following equation shows the final energy loss equation that is a function only of water equivalent depth

$$E_{\mu loss} = 5.31 * 10^{-14} d^{2.95} - \frac{10^{6.0}}{d} + 12 \tag{3}$$

where d is the total depth in centimeters water equivalent. The numbers in this equation could be different depending on the optimization method used, and in this case, were optimized by minimizing the error between the measured flux at six mine depths and the prediction. After the muon energy loss equation was determined, it was necessary to make a function that accurately represented the hydrostatic depth. This equation needed to be a function of the physical depth, reservoir thickness and porosity, and CO_2 density. The CO_2 density was represented as a piecewise function of the three possible phases present: gas, liquid, and supercritical. The water equivalent well depth will be a function which changes according to the amount of CO_2 present in the reservoir. The change is caused by subtracting off water equivalent depth or adding water

equivalent depth as the density decreases or increases. A function which performs this density based depth correction is given by

$$d = cmwe - rd * (\rho_{res}(0, 0, p, cmwe) - \rho_{res}(\varepsilon, x_{co2}, p, cmwe)) \quad (4)$$

where *cmwe* is centimeters of water equivalent to the well bottom, x_{co2} is the CO_2 saturation, and *rd* is the reservoir thickness. ρ_{res} is the density of the reservoir in grams/cm^3, including CO_2 saturation, given by Equation 5,

$$\rho_{res}(\varepsilon, x_{co2}, p, d) = (1 - \varepsilon)\frac{d}{p} + (1 - x_{co2})\,\varepsilon\,\rho_{brine} + x_{co2}\,\varepsilon\,(0.0523\ln(d) + 0.1009) \quad (5)$$

where p is the physical depth of the well in centimeters water equivalent, ε is the porosity, and ρ_{brine} is the density of the brine in grams/cm^3.

Figure 2.6 shows the results of Method 1 as compared to muon measurements made at six mine depths (Gray et al., 2011). This method produces an average error of 7.7% for these particular mines. The values compared in Figure 2.6 are for zero saturation, so the water equivalent depths are equal between the measured and computed flux values.

Method 2

The second method is less complex than Method 1. Mei and Hime (2006) developed the following empirical function for the flux at depth

$$I_\mu = 67.97 * 10^{-6} e^{-\frac{d}{0.285}} + 2.071 * 10^{-6} e^{-\frac{d}{0.698}} \quad (6)$$

where d is the depth in kilometers water equivalent. This equation has an average error of 0.5% when compared with measured flux values. However, it is only a function of kilometers water equivalent, rather than a function of physical depth and density, reservoir thickness and porosity, and CO_2 saturation. The equation can be transformed to include these parameters by substituting the previously derived Equation 4 into Equation 6, which describes the effective water equivalent depth d. The two methods were then used to predict changes in the flux at the mine depths given a 50% loss of CO_2 saturation in a 20% porosity reservoir with three reservoir thicknesses.

Table 2.1 shows the flux changes predicted by Methods 1 and 2 for 10, 30, and 100 m reservoir thicknesses. As previously stated, each value corresponds to a 50% change in CO_2 saturation of a 20% porosity reservoir. The predictions for the change in flux are very similar between Methods 1 and 2. The calculations in the table show that the equations derived for Method 1 give similar results to the Mei and Hime empirical formula. Additionally, the similarity of the results for the two methods give more confidence in the results of both. The results also illustrate the necessity of having a very accurate detector, as the flux changes will be quite small. For example, even a 50% change in CO_2 saturation in a 30-m thick reservoir at 1.6 km hydrostatic depth will change the flux by only 0.6%. Thus, the detector must obtain a sampling of the muon flux with an uncertainty less than 0.6% to resolve saturation changes.

Muon Detection and Existing Designs

Muons are not difficult particles to detect. They leave a fairly consistent energy trail of approximately 2 MeV cm^2/g. They interact through the weak and electromagnetic forces, and as discussed, the majority of muons will undergo primarily ionization and bremsstrahlung processes. Electrons are similar in that they also deposit a fairly uniform amount of energy. However, the signals from electrons can be discriminated from that due to muons in a detector. A muon will not incur appreciable angular deflection, unlike an electron. Muons are also much heavier, and will almost always have significantly more energy. Thus, in a detector, a straight line of deposited energy is most likely a muon. Cloud chambers can be used to differentiate muons from electrons because of their straight path (Rochester et al., 1953; Nishiyama et al., 2015), while electrons take a very circuitous path.

Muon detector designs are generally based on drift tubes (Bittner et al., 2011; Guardincerri et al., 2015), cathode strips (Acosta et al., 2008), or scintillators (Alfaro et al., 2010; Aguayo et al., 2013). Drift tubes use ionizable gas filled chambers with an applied voltage between the center rod and outer cylindrical encasing. The particle passing through the tube leaves a trail of ionized electrons that are collected at the anode. The amount of time it takes the gas to be ionized and pass through the chamber is how the drift tube electronics can calculate the approximate position of the event. This process makes them more susceptible to changes in

temperature and fluctuations in supplied power. These attributes also make them undesirable for deployment underground.

Cathode strip chambers, such as the ones on the compact muon solenoid at CERN (Acosta et al., 2000), work on a similar principle to drift tubes in that they use an ionizable gas and electrodes. However, the chamber consists of orthogonal layers of cathode strips and anode wires that can give two coordinate positions of the muon passing through. Thus, cathode strip chambers do not rely on timing for position, but provide that information based on their intrinsic design. Ultimately they were not chosen for this underground application because they still suffer from changes with temperature and require high-voltage power supplies to operate.

Scintillation detectors use fluour doped polystyrene or polyvinyltoluene to generate light as particles pass through the medium. As the light photons scatter in all directions, some of them can be collected by PMTs placed in geometrically sensible positions. Scintillating plastics are largely insensitive to temperature changes, and are low maintenance detection systems. However, they do not have good resolution, and the detector will be essentially unable to determine the incoming particle energy. As this application will need only angular data, not energy, scintillating material was the chosen design for this borehole muon detector. The detector design is low maintenance, temperature insensitive, and can be made small enough to fit in the borehole while still providing the necessary angular information. An orthogonal arrangement of scintillating rods, similar to a cathode strip chamber, will provide multiple coordinate points. In the detector designed in this thesis, the scintillating material is rods made of polystyrene doped with POP (2,5-diphenyloxazole) and POPOP (1,4-bis benzene) fluours and coated with titanium dioxide on all sides, leaving the ends bare. Thus, the light collection for this design occurs at the ends of the rods. The titanium dioxide coating is in place to minimize light loss and cross-talk between adjacent rods. The primary difficulty of the design is the necessary front-end electronics to capture the photons produced.

Tomographic Imaging

As previously discussed, it is possible to obtain detailed information about rock formations using muon detection. Muon tomography is the reconstruction of this data to form a

tomographic image of the region of interest. One notable success with this imaging method was performed on Mt. Asama by a research group in Japan (Tanaka et al., 2001). Depending on the detector used, the image constructed from the signal generated can be very accurate. The angular resolution of the detector will determine the spatial resolution of the tomographic image. Such an image is the result of a large number of muon events detected over a period of time. Each muon event is recorded at a particular angle, and a histogram of the number of muons recorded at that particular angle is generated. The angle is associated with a path length through the overburden. The total muon flux at that angle is compared with the expected flux from a known sea-level spectrum. Any difference from the known spectrum provides the needed reference point to determine the thickness of the overburden. The calculated overburden thickness over the solid angle of the detector produces a tomographic image. The reproduction of this image over time, and the associated changes in the tomography, is the basis for monitoring underground sequestration reservoirs. Over time, maybe weeks and months, the image will be reproduced, showing changes in the tomographic image, providing information as to the shift of the CO_2 plume and changes in reservoir CO_2 saturation.

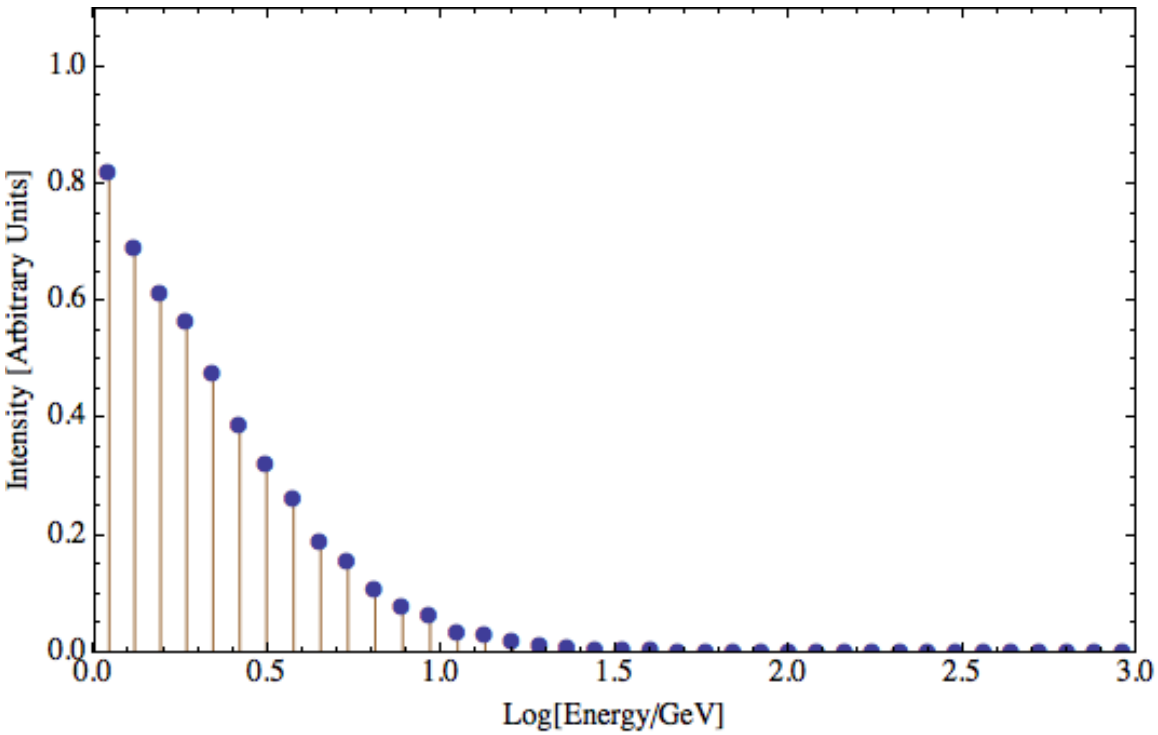

Figure 2.1: Muon sea level energy spectrum as produced in a CRY simulation.

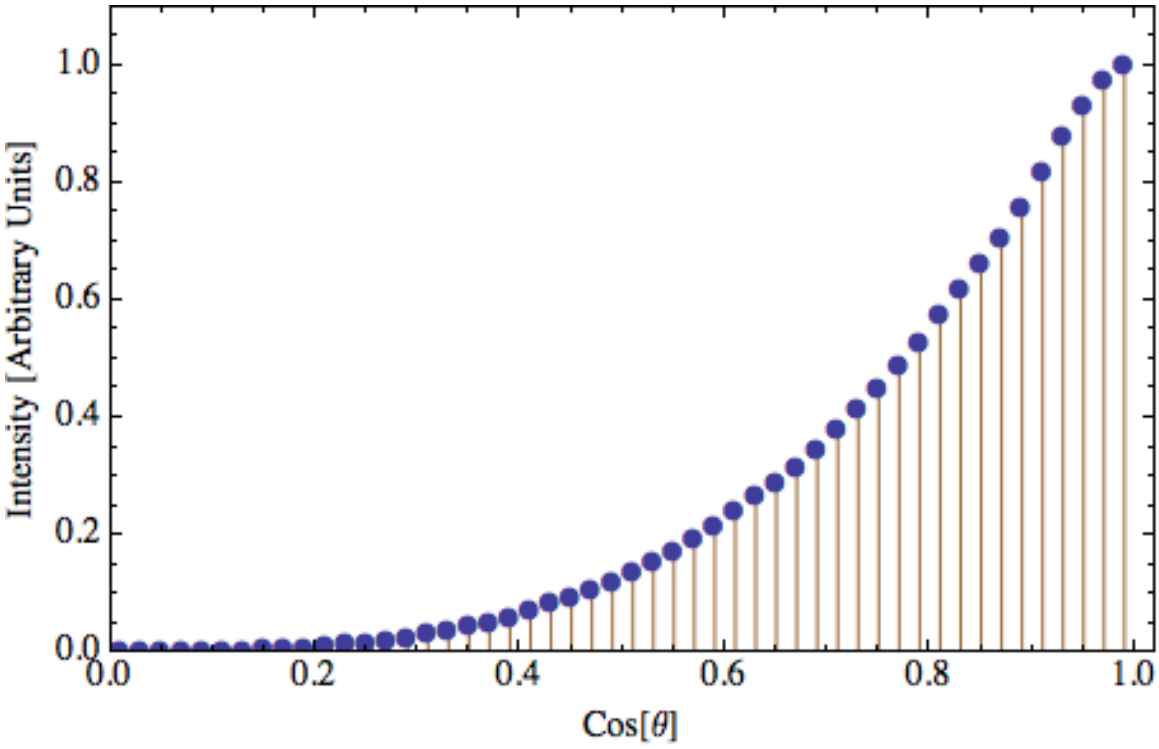

Figure 2.2: Muon sea level angular spectrum produced in a CRY simulation.

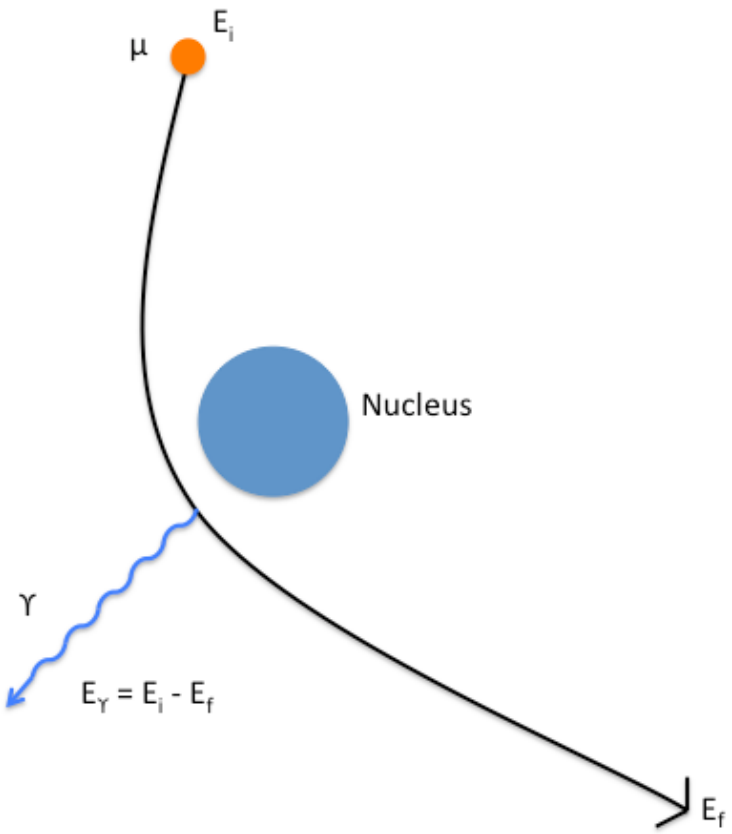

Figure 2.3: The basic process of bremsstrahlung radiation emission.

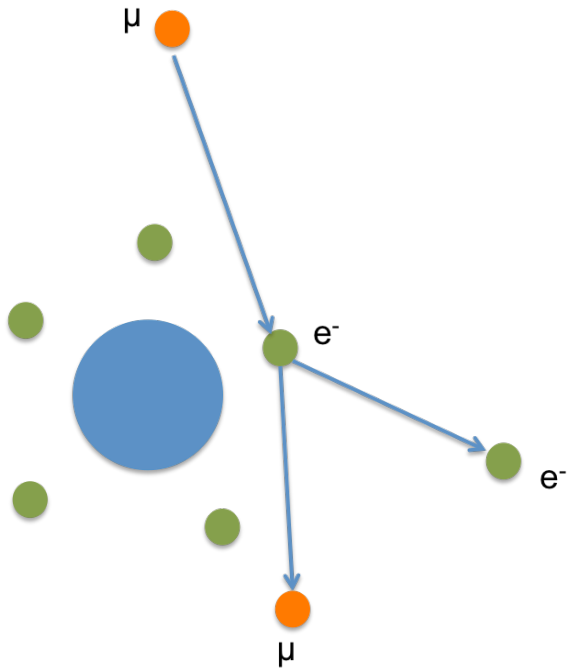

Figure 2.4: Basic ionization process. Results in the generation of an energetic electron which can cause a cascade of further bremsstrahlung and ionization events.

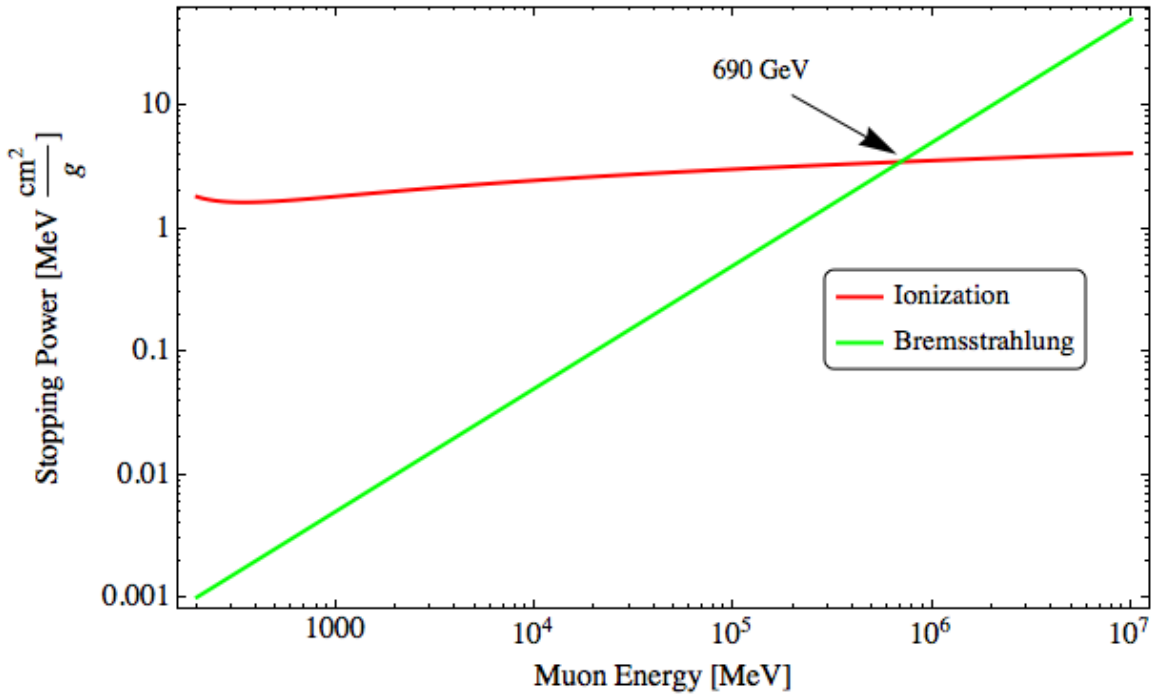

Figure 2.5: Muon energy loss contributions from ionization and bremsstrahlung. The critical energy occurs where bremsstrahlung overtakes ionization, marked at 690 GeV on the graph. The parameters used in the equations were for standard rock (Z/A = .500).

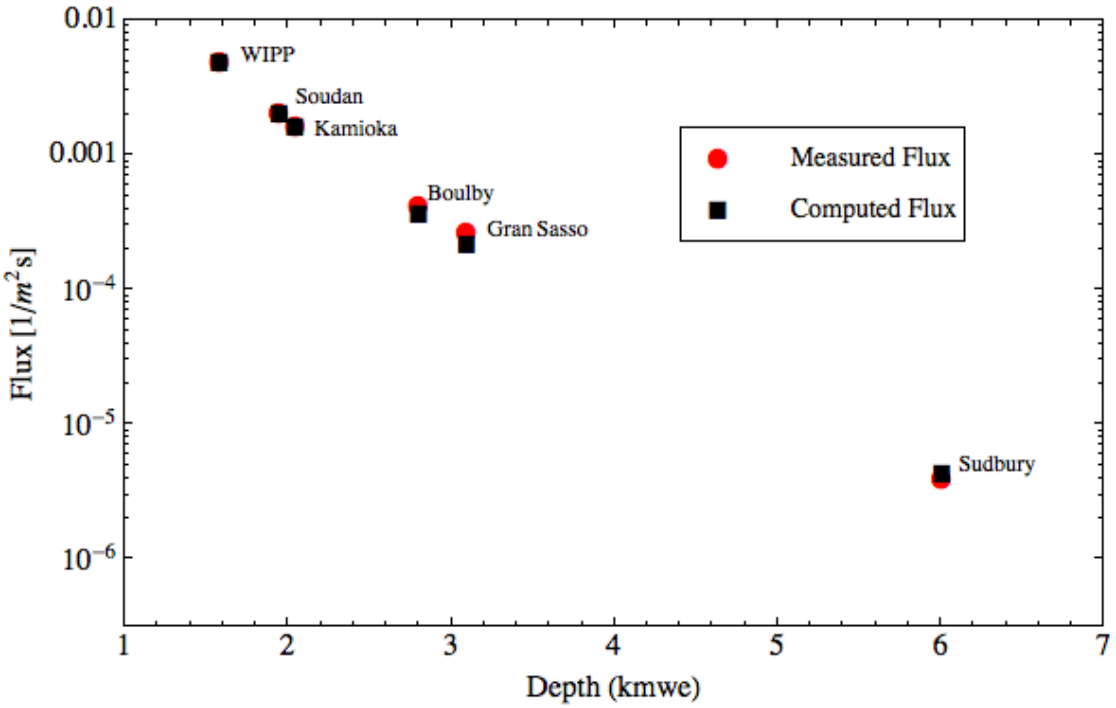

Figure 2.6: Measured and computed flux in the WIPP, Soudan, Kamioka, Boulby, Gran Sasso, and Sudbury mines. The mines are ordered from shallowest to deepest and the flux at each location was computed using Method 1, which produced an average error of 7.7% for these six mines.

Table 2.1: Percent flux change for a 20% porosity reservoir at 6 mine depths with a 50% loss in CO_2 saturation.

		Percent Flux Change					
		10 m reservoir		**30 m reservoir**		**100 m reservoir**	
	Depth (k.m.w.e.)	Met. 1	Met. 2	Met. 1	Met. 2	Met. 1	Met. 2
WIPP	1.585	0.23%	0.23%	0.71%	0.69%	2.41%	2.33%
Soudan	1.95	0.18%	0.17%	0.54%	0.53%	1.82%	1.78%
Kamioka	2.05	0.08%	0.08%	0.24%	0.23%	0.79%	0.77%
Boulby	2.805	0.06%	0.05%	0.18%	0.16%	0.61%	0.54%
Gran Sasso	3.05	0.06%	0.05%	0.17%	0.15%	0.56%	0.51%
Sudbury	6.011	0.03%	0.04%	0.10%	0.13%	0.32%	0.42%

References

Acosta, D.; Apollinari, G.; Blomquist, J.; Breedon, R.; Bondar, N.; Bonushkin, Y.; Borissov, E.; Bujak, A.; Bylsma, B.; Chester, N.; et al. *Large CMS Cathode Strip Chambers : Design and Performance*; 2000; Vol. 453.

Acosta, D.; Adam, A.; Andreev, V.; Apollinari, G.; Baek, Y.; Banicz, K.; Barashko, V.; Barberis, E.; Bartalini, P.; Bloch, I.; et al. Efficiency of Finding Muon Track Trigger Primitives in CMS Cathode Strip Chambers. *Nucl. Instruments Methods Phys. Res. Sect. A Accel. Spectrometers, Detect. Assoc. Equip.* **2008**, *592* (1-2), 26–37.

Aguayo, E.; Fast, J. E.; Kouzes, R. T.; Orrell, J. L. The Muon Witness Detector : A Ruggedized , Portable , Flux Meter for Cosmogenic Activation Monitoring. *IEEE Trans. Nucl. Sci.* **2013**, *60* (2), 689–692.

Alfaro, R.; De Donato, C.; D'Olivo, J. C.; Guzmán, a.; Medina-Tanco, G.; Moreno Barbosa, E.; Paic, G.; Patiño Salazar, E.; Salazar Ibarguen, H.; Sánchez, F.; et al. Buried Plastic Scintillator Muon Telescope (BATATA). *Nucl. Instruments Methods Phys. Res. Sect. A Accel. Spectrometers, Detect. Assoc. Equip.* **2010**, *617* (1-3), 511–514.

Andreev, Y. M.; Bugaev, E. V. Muon Bremsstrahlung on Heavy Atoms. *Phys. Rev. D* **1997**, *55* (3).

Berghaus for the IceCube Collaboration, P. Direct Measurement of the Atmospheric Muon Energy Spectrum with IceCube. *Proc. 31st ICRC* **2009**, *10*, 4.

Bethe, H.; Heitler, W. On the Stopping of Fast Particles and on the Creation of Positive Electrons. *Proc. R. Soc. London* **1934**.

Bittner, B.; Dubbert, J.; Horvat, S.; Kortner, O.; Kroha, H.; Legger, F.; Richter, R.; Adomeit, S.; Biebel, O.; Engl, A.; et al. Development of Fast High-Resolution Muon Drift-Tube Detectors for High Counting Rates. *Nucl. Instruments Methods Phys. Res. Sect. A Accel. Spectrometers, Detect. Assoc. Equip.* **2011**, *628* (1), 154–157.

Bugaev, E. V.; Shlepin, Y. V. Photonuclear Interaction of High Energy Muons and Tau Leptons. *Phys. Rev. D* **2003**, *67* (3), 1–12.

Cullerne, J. The Penguin Dictionary of Physics; Penguin: London, United Kingdom, 2009.

Drury, L. O. C. Origin of Cosmic Rays. *Astropart. Phys*. 2012, pp 52–60.

Gaisser, T. K. Spectrum of Cosmic-Ray Nucleons, Kaon Production, and the Atmospheric Muon Charge Ratio. *Astropart. Phys.* **2012**, *35* (12), 801–806.

Gray, F. E.; Ruybal, C.; Totushek, J.; Mei, D. M.; Thomas, K.; Zhang, C. Cosmic Ray Muon Flux at the Sanford Underground Laboratory at Homestake. *Nucl. Instruments Methods Phys. Res. Sect. A Accel. Spectrometers, Detect. Assoc. Equip.* **2011**, *638* (1), 63–66.

Griffiths, D. J. *Introduction to Elementary Particles*, 2nd ed.; John Wiley & Sons, Inc., 1987.

Guardincerri, E.; Bacon, J.; Borozdin, K.; Matthew Durham, J.; Fabritius II, J.; Hecht, A.; Milner, E. C.; Miyadera, H.; Morris, C. L.; Perry, J.; et al. Detecting Special Nuclear Material Using Muon-Induced Neutron Emission. *Nucl. Instruments Methods Phys. Res. Sect. A Accel. Spectrometers, Detect. Assoc. Equip.* **2015**, *789*, 109–113.

Hagmann, C.; Lange, D.; Wright, D. Cosmic-Ray Shower Generator (CRY) for Monte Carlo Transport Codes. *Nucl. Sci. Symp. Conf. Rec. 2007. NSS'07. IEEE* **2007**, *2*, 1143–1146.

Macluc, F.; Grupen, C.; Hashim, N. O.; Luitz, S.; Mailov, a.; Müller, a. S.; Putzer, a.; Sander, H. G.; Schmeling, S.; Schmelling, M.; et al. Muon-Pair Production by Atmospheric Muons in CosmoALEPH. *Phys. Rev. Lett.* **2006**, *96* (2), 1–4.

Mei, D. M.; Hime, A. Muon-Induced Background Study for Underground Laboratories. *Phys. Rev. D. Cosmol.* **2006**, *73* (December 2005), 1–18.

Nakamura, K.; et al. Passage of Particles through Matter. *J. Phys.* **2010**, *G* (37), 075021.

Nishiyama, R.; Miyamoto, S.; Naganawa, N. Application of Emulsion Cloud Chamber to Cosmic-Ray Muon Radiography. *Radiat. Meas.* **2015**, *83*, 56–58.

Olive, K. A.; Agashe, K.; Amsler, C.; Antonelli, M.; Arguin, J.-F.; Asner, D. M.; Baer, H. *Particle Physics Booklet*; 2014; Vol. 38, pp 262-264.

Rebef, H.; Sima, O. The Muon Charge Ratio in Cosmic Ray Air Showers. In *AIP Conference Proceedings*; 2008; Vol. 972, pp 338–346.

Rochester, G. D.; Wilson, J. G.; Liddel, U. Cloud Chamber Photographs of the Cosmic Radiation. *Phys. Today* **1953**, *6* (8), 16.

Tanaka, H.; Nagamine, K.; Kawamura, N.; Nakamura, S. N.; Ishida, K.; Shimomura, K. Development of the Cosmic-Ray Muon Detection System for Probing Internal-Structure of a Volcano. In *Hyperfine Interactions*; 2001; Vol. 138, pp 521–526.

CHAPTER 3

SIMULATION AND DESIGN

An accurate simulation of the muon borehole detector is critical to understanding and predicting the detector response, as well as testing different designs. The detector is composed of square polystyrene rods, fitted with wavelength shifting fibers internally to transport the light to the photodetector. The simulation can be used for predictions with different configurations. It can allow the angular resolution of the detector to be computed, the energy deposition as a function of incoming muon angle, and the effects of secondary particle generation. Each of the rods is monitored by the simulation to detect energy deposition, as well as particle angle and type.

The simulation package used was Geant4, an advanced Monte Carlo-based code developed by CERN (Agostinelli et al., 2003). Geant4 is particularly good for high-energy applications, as it was developed specifically for the Large Hadron Collider, including the Atlas and Compact Muon Solenoid detectors. The cosmic muon spectrum is high-energy, with the majority of muons well above 1 GeV, which makes Geant4 an appropriate simulation package.

Simulation Physics

The physics engine of Geant4 is versatile, with multiple implementations at various energies. The physics package chosen by the research group for this simulation uses a Fritiof high-energy model and a Bertini cascade (Yarba, 2012) for the lower energies, as well as the Geant4 standard electromagnetic physics, all of which have substantial verification (Apostolakis et al., 2010; Yarba, 2012). The Fritiof physics package is a high-energy string model. This provides the framework for all hadronic interactions greater than 4 GeV, including high-energy inelastic collisions. The Bertini cascade model is also a hadronic interaction model based on particle-particle collisions, and works well at intermediate energies below 5 GeV. Included in the

physics package, and the most vital part of the physics engine, is an entire electromagnetic interactions library of cross sections and particles from the keV to the PeV range (Amako et al., 2005).

As described in the Muon-Matter Interactions section in Chapter 1, when a muon passes through matter, it has multiple pathways of interaction. The types and relative frequency of these interactions, modeled as stochastic processes, will determine much about the detector performance and related errors.

Design Concept

Figure 3.1 shows the design concept of the detector. The detector will ultimately be placed underground in a borehole at 1-2 km deep. Its purpose is to monitor density changes in the overburden (rock formations) above the buried detector using changes in the detected muon flux. Its design will need to be less than about 20 cm in diameter and about 1 m in length. The detector will be encased in a noncorrosive metal pipe for protection. The basic concept of the design in Figure 3.1 is the use of four layers of scintillating rods arranged in orthogonal layers to provide a coordinate system to determine the angle of the incoming muon. The scintillating rods will be fitted with wavelength shifting fibers. The fibers will be coupled to silicon photo-multipliers for light collection and the onboard electronics will be used for postprocessing. The two most important design concepts are the angular resolution and the surface area. If either the angular resolution is increased (angular error decreased) or the surface area is increased, it will increase the statistical certainty of the measurements, which will decrease the measuring time required.

Detector Numbering Scheme

Figure 3.1 shows the full 4-layer detector design with the associated bar numbering scheme. While this configuration is not the first one that was simulated the figure is shown first so that it is understood in the figures to follow which bar number corresponds to which layer, and their respective orientation. It will be important to examine the energy deposition in individual bars, single layers, double layers, and the full design. This will provide insight to the role that

secondaries play in the detector performance, as well as understanding the postprocessing methods to follow.

Simulation Details

The simulation of the 4-layer detector consists of 170 polystyrene rods, each 1 cm x 1 cm in cross section, with lengths of either 70 cm or 15 cm. The rods are arranged in alternating layers of 15 long rods, each 70 cm long, and 70 short rods, each 15 cm long. The layers, as shown in Figure 3.1, are arranged in orthogonal layers, with a space between the inner two layers. Simulations used spacing ranging from 0 cm to 15 cm. The larger the spacing, the lower the angular error of the detector and the lower the efficiency. In each case, the spacing of the particular simulation will be mentioned.

The Geant4 simulation was coded to keep track of all primary and secondary interactions during each event. A primary interaction is the interaction of a primary particle, or the particle generated by the source, and secondary interactions are from particles generated by primary particles interactions with the detector. When a particle interacts with the detector and deposits energy, the simulation tracks it as a “hit” on the detector. All the particle information and their hits are loaded into arrays called hits collections, which contain the information about each hit, what type of particle it was, how much energy it deposited, and the global timing of the hit. Additional information includes the momentum vector of the primary muon, meaning the momentum of the muon generated by the source. These data were written to a file, and imported into Mathematica for postprocessing. The post-processing, and the specifics of the output file, are discussed in the Postprocessing techniques section.

Expected Insights

The angular resolution of the detector will provide a basis for further calculations on the ability of the detector to resolve changes in the total flux and the flux as a function of angle. The angular flux will be less pixelated with a greater detector resolution (meaning smaller angle of error). The detector will then be able to more effectively “bin” the incoming muons, providing a better statistical premise for the detection of changes in angular flux. The particular insights

needed from the simulation include the following effects on the angular resolution: secondary particle generation within the detector, shielding, postprocessing techniques, and background.

When a muon interacts with the detector material, it will generate a cascade of secondary particles. Ideally, most of these secondary particles will be immediately absorbed into the material and detected as the energy deposited by the muon in the same bar in which the secondaries were generated. However, it will be possible for high-energy secondary particles to travel to different bars, and even to different layers of bars. If the energy deposited by these particles is greater than the muon energy deposit, it will be registered as the primary hit. If a secondary particle is registered as the primary hit, the detector electronics will calculate an incorrect angle for the muon. To mitigate the number of secondary particles causing hits on the lower layer of the detector, shielding was investigated as a solution, and was found to produce a negligible benefit. The shielding tended to produce as many secondaries as it absorbed, due to interactions of the muons with the dense shielding material, cancelling out the positive effect. Shielding is discussed further in the Shielding and Secondary Particle Generation section of this chapter. Eventually, it was required to cancel the effects of secondary particles by using post-processing techniques as discussed in the Postprocessing section also in this chapter.

Preliminary Simulations

The initial simulations were performed with a simple, single bar model, where effects such as incident muon angle and secondary particle production can be seen clearly. It was found that a muon would deposit on average about 2 MeV in a 1 cm rod of polystyrene (approximately 1 g/cm^3). Figure 3.2 shows a mono-energetic positive muon beam (1 cm x 1 cm) incident on a single polystyrene rod, with an average deposition of 1.93 MeV from 10^5 muons, and an uncertainty of less than 8 keV.

Vertically incident muons will pass through approximately 1 cm of the rod, whereas angled muons can have a longer or shorter path length, leading to a spread in the energy deposition. If this same beam is tiled to 45 degrees from vertical (as shown in Figure 3.2), the energy deposition histogram shown in Figure 3.3 is obtained. The shape of the histogram in Figure 3.3 shows that the muon deposits energy in proportion to the path length through the rod.

Thus, when a full angular and energy spectrum is used, it can be expected that there will be a wide range of energy deposited per rod due to varying path lengths. Depending on the angle, the muon could travel through the hypotenuse of the rod or merely glance an edge. The glances through the edges are what cause the flat section of energy deposition in Figure 3.3 below approximately 2.3 MeV. The long tail to the right is from the few muons that hit through or near the hypotenuse of the rod and/or undergo a more infrequent physical process, such as pair-production (Macluc et al., 2006).

The energy of the incoming muon deserves careful attention, as the energy spectrum of muons at both the Earth's surface, and at depth, contains a large spread of energies. Figure 3.4 shows the energy deposited by a vertically incident beam of muons at energies ranging from 100 MeV to 1 TeV. The simulations were performed with μ+, although μ- are present as well at the surface and at depth. The muon charge ratio is ~1.25 μ+/μ- as discussed in Chapter 2. Figure 3.4 includes the energy deposition of negative muons as well as positive, each from simulations of 10^5 particles. The μ+ and μ- have the same energy deposition at every energy, with an average deviation of only 0.1%. Thus, the type of muon is of scientific interest, particularly due to Bohr radius trapping and slight differences in decay lifetimes, but not of practical significance in these simulations. The negative muon has a shorter measurable decay lifetime not because the decay mechanism is any different (Mulhauser, 2006), but because the negative muon has a probability of being stabilized in a Bohr radius and lengthening out the lifetime.

Across the majority of the muon energy spectrum, it can be expected that about 1.95 MeV will be deposited in the polystyrene bars. Both radiative and ionization loss procedures are included in this value. The additive ionization and radiative energy loss processes, as well as extensive energy loss data tables for various energies and materials are presented in the literature (Lohmann et al., 1985). The simulation keeps track of ionization and bremsstrahlung events by tracking secondary particles. However, because this simulation did not study these effects disparately, the energy deposited in each simulation will include both.

After the single bar simulations the model was extended to a single layer of bars, each 1 cm x 1 cm. Figure 3.5 shows the model of a single 1 x 15 layer of long rods. The response of the

rods to an incoming muon will be important in determining postprocessing needs, as well as energy discrimination parameters in the electronics. The next simulation was performed to investigate the energy deposition from a highly tilted muon beam, and the results showing the average energy deposition per rod per muon are presented in Figure 3.6. The muon beam was tiled to approximately 82 degrees from vertical, and shows the contributions from secondary particles as well as the primary muons.

On average, the secondaries only deposit about 10-20% of the total deposited energy per interaction. In this single layer simulation, it is possible to see the effect of secondary particles being produced and traveling to other bars. Migration of secondary particles is of particular significance in multilayer simulations, where the secondaries can travel between layers, creating both errant energy deposits and potential timing complications. Figure 3.7 shows a 2-layer model, where the top layer is 15 rods each 70 cm long. The orthogonal layer shown below is made of 70 rods each 15 cm long. It is important to note that the simulations performed with 2-layer models differ slightly from the numbering convention in that the second orthogonal layer is numbered 16-75. This does not affect any calculations, as none are performed on this two-layer design, but is merely for qualitative understanding of the graphs to follow. The two-layer simulation provides valuable insight into the effect of secondary particles as the number of layers increases, as well as determining the effect of shielding between layers.

The results from Figure 3.7 allowed the effects of placing shielding between rod layers. A 5-mm sheet of lead was placed equidistant between the two layers and the results of the subsequent simulation is shown in Figure 3.8. It was expected that the lead would absorb nearly all secondary particles. However, the interaction of the electrons with the lead will cause some bremsstrahlung events. The gamma rays produced through bremsstrahlung, however, should not be a large factor, as their energy deposition is small. The 5-mm layer of lead shielding absorbed the majority of the secondary particles incident, however, the number of secondary particles absorbed in the shield was offset by the number of secondary particles produced when the muon passed through the shield. This is evident from comparison of Figures 3.7 and 3.8, which are nearly identical, particularly in rods 59-62 in the lower layer where the muon had direct

interactions. As expected, there was a slight thinning of the energy deposited spuriously in far-away rods with shielding in place, but these contributions were small and made no significant effect on the detector performance. The effects of shielding will be revisited in the Post-Processing section to give the quantified effect on angular resolution.

Full-scale Simulations

Full-scale simulations will be used to further understand the response of the detector in more realistic simulations. The full-scale simulations will use the full 4-layer detector and will eventually incorporate the naturally occurring cosmic muon spectrum into the source. Once the simulations were completed, the results were processed in a way to simulate the electronics that will be used. The electronics will be capable of performing both threshold and coincidence discrimination and are discussed in depth in the Postprocessing section in this chapter. From the full-scale simulations, the angular resolution of the detector was determined at various detector configurations. Additionally, the effects of the outer encasing pipe were explored, and potential future design optimizations are presented.

This section will start with a simple simulation performed on the 4-layer design. Figure 3.9 shows the full 4-layer simulation with a single monoenergetic muon beam passing through all 4 layers at an angle. It also shows the energy deposition per bar and the relative contributions to the total energy from primary muons and from secondary particles. The distinct peaks seen in Figure 3.9 suggest that the detector layers should respond (on average) predictably to a muon event. The muons themselves should deposit far more energy than any secondaries, including those produced that travel to other bars. From the Geant4 graphic in Figure 3.9, it would appear that a portion of secondaries produced travel randomly to other locations in the detector. While this is certainly occurring, it is, from the graph in Figure 3.9, a rarer event than the secondaries being absorbed into the same bar (or a closely adjacent bar) the muon passed through. After the response of the detector was well understood, including the contributions from various particles, the angular resolution was determined using the methods described in the Postprocessing section.

Postprocessing

In order to quantify the angular resolution of the full-scale detector, a postprocessing methodology was developed. Two methods were used to determine the angular resolution of the detector. The first method used the bar location with the maximum energy deposition to calculate the incident angle of the muon. The second method relied upon an energy weighted average position in each layer. Using the energy deposition per rod and the location of the rod, it is possible to extract a computed angle from the detector, which can then be compared to the true angle from the momentum vector. Table 3.1 shows a single event from the output of the simulation in Figure 3.9. The first column is the energy deposited, in MeV, from any event, whether primary muon or secondary. The second column is the rod number according to the aforementioned scheme, and the third is the absolute time of the event in nanoseconds. Time is counted from the moment the muon is generated at the particle source to when the muon is either absorbed in a material or passes out of the defined world volume in Geant4. For these simulations, with the energy of the muons being high, only very few muons are killed before exiting the world volume. The Particle Data Group (PDG) encoding column contains the particle identification number, according to established particle physics abbreviations. Muons are signified by 13, and electrons by 11, where the negative correlates to the antiparticle. The last row of every event is filled by the 3-D muon momentum vector (as obtained in the top layer by the simulation) and followed by -100000, which signifies the end of an event.

Both methods previously discussed eventually compute the zenith angle from Equation 7, as derived from Figure 3.10.

$$zenith = \frac{\pi}{2} - \theta = \frac{\pi}{2} - tan^{-1}\left(\frac{\sqrt{(x_2 - x_1)^2 + (z_2 - z_1)^2}}{y_2 - y_1}\right) \quad (7)$$

Where x, y, and z values correspond to individual rods according to the coordinate system in Figure 3.10, and θ is the angle normal to the top surface of the detector. The y values are taken in the middle of the two layers, as Figure 3.10 shows. This is the best location to assume and is 11 cm in the simulation shown. A code was written in the Mathematica programming language (Wolfram, 2012) to parse the output and calculate the computed angle of

each event. This computed angle was then compared to the known angle from the muon momentum vector. The difference between these two values, in degrees, will be referred to as the angular error. To compare the two methods, Table 3.2 shows the positions used in each calculation, where the average energy weighted position is given by Equation 8, which applies to x and z dimensions.

$$x_{avg} = \frac{\sum_i x_i E_i}{\sum_i x_i} \tag{8}$$

These values, from Table 3.1, resulted in angle calculations of 42.41 and 41.47 for the maximum and averaged, respectively. These are both in good agreement with the real muon angle of 41.47. However, the error on the averaged calculation is smaller, which will be shown to consistently be the case. Figure 3.11 shows the angular error as a histogram for the averaged calculation from a simulation of $3*10^5$ muons, with a layer spacing of 11 cm. The overall distribution has a mean of 0.97 and a median of 0.62 degrees. Only 1.2% of the muon events measured had greater than a 5 degree angular error.

Shielding and Secondary Particle Generation

It is shown in Figure 3.11 that there are only a few events with errors greater than approximately 10. In order to investigate this issue, an additional section of code in Mathematica was written by that extracts the event responsible for the maximum error. For one particular simulation, the maximum error was approximately 48 degrees and was caused by the event shown in Figure 3.12. The secondary particles produced in this event forced a completely vertical computed angle of 90 degrees. This was approximately 48 degrees off of the actual muon, coming in at approximately 42 degrees. However, this was the highest error of over 10^5 muon events. Shielding between the layers was proposed as a means of absorbing secondary particles that would otherwise travel to other layers, causing random energy depositions. The results of the same muon beam used in Figure 3.9 are shown in Figure 3.13, which is analogous to the histogram in Figure 3.11, except with shielding. The picture in Figure 3.13 clearly shows that although many secondaries from the upper layers are absorbed in the shield (which are spurious electrons), the shield itself produces additional secondaries. The two effects essentially cancel

each other out, and shielding makes a negligible difference in the computed angles, as shown in Table 3.3.

When the detector is deployed underground, it will be placed in a 0.5 in. thick stainless steel pipe. The pipe will slightly change the response of the detector through the production of additional secondaries. However, the pipe will also shield the detector from subterranean background. The response of the detector with the surrounding pipe (Figure 3.14) is shown in Table 3.4, which indicates that the effect from the pipe is noticeable, but not significant, with a mean decrease in detector accuracy of approximately 1 degree. However, when the detector is underground, it will receive many more secondaries and subterranean background than was previously simulated, the effects of which are discussed in the Subterranean Background section.

Until the results in Table 3.3, only mono-energetic and single angle muon beams were used. When muons approach the earth, they do so from many angles and with many energies. As they pass into the surface of the earth, the energy and angular spectra change and continue to favor straighter angles and higher energies as depth increases. The section on muon production shows these spectra at various depths. Figure 3.15 shows a muon spectra incident on the detector (with the underground encasing) at 1500-m water equivalent.

With the full spectra at 1500-m water equivalent, the mean and median angular errors are 1.66 and 0.77 degrees, respectively. Even with the stainless steel encasing, the angular errors are less than 2 degrees. With angular errors of only 1-2 degrees, the detector will be able to successfully “bin” incoming muons by angle, increasing its ability to resolve overburden thickness changes.

Once the detector is placed underground, it is likely that it will not be perfectly oriented with the detector surface parallel with the Earth surface. The effect this will have on the angular resolution of the detector has been determined. A series of simulations were performed, each with more than 10^5 particles, where the angle between the detector and the muon source was changed to reflect a tilted detector placement. Figure 3.16 is a graphic of the simulation with the muon source at a 45 degree angle to the detector. In this case, 90 degrees represents the detector surface normal to downward muons, as in Figure 3.15.

Interestingly, the median error changes less than 1 degree over the whole range of angles. Even if the detector surface is placed completely orthogonal to the downward muons, the error in the readings remains similar. However, what is not shown here is the significant decrease in overall detected flux. If the detector is oriented orthogonal to the downward muons, the coincidence count rate is expected to decrease by approximately two orders of magnitude. This would be an unacceptable problem to occur in a horizontal well. One of the major design considerations is the maximization of coincident events, creating better statistics to work with in resolving overburden thickness changes.

Figure 3.17 shows the effect on the overall detector efficiency (the amount of flux detected) and angular error with different spacing between the inner layers. Geometrically, the detector becomes better able to resolve the muon angle when the layers are spaced further apart, decreasing the angular error. However, the greater the spacing between the layers, the lower the detector efficiency, as shown in Figure 3.17. Thus, the detector design will need to balance angular error with the required efficiency. At deeper boreholes, it will be necessary to maximize the detector efficiency due to the extremely low flux.

More Isotropic Design

The aforementioned results of detector orientation sparked a few new design considerations, such as the possibility of making a detector that is isotropic. Figure 3.18 shows the first design that uses a more circular approach. This design was known not to be isotropic, but it is slightly better than the 4-layer detector shown until now. One of the issues with the 4-layer detector is that the minimum angle of approach of a muon in order to cause coincidence is 45 degrees. Figure 3.18 shows a detector design based on semicircular outer rods 1 cm thick surrounding two layers of 10-1 cm rods.

The minimum muon approach angle for this design is 17 degrees, which is an improvement over the 4-layer design, and will allow a greater flux to be measured. This is primarily due to the spacing between the two inner layers being only 3 cm. Additionally, this design still provides an angular resolution of approximately 3 degrees. The postprocessing of this type of detector design was more complex than the previous design. In order to calculate the

positions for angular computation, it was necessary to calculate the exact position of the muon hit on the semicircular rods. The resulting formulae, Equations 9 and 10, used to calculate the x and y values are as follows:

$$x'_{1,2} = \frac{(y_1 - y_2)(x_2\,y_1 - x_1\,y_2) \pm \sqrt{(x_1 - x_2)^2(r^2((x_1 - x_2)^2 + (y_1 - y_2)^2) - (x_2\,y_1 - x_1\,y_2)^2)}}{(x_1 - x_2)^2 + (y_1 - y_2)^2} \quad (9)$$

$$y'_{1,2} = \frac{(x_1 - x_2)(x_1\,y_2 - x_2\,y_1) \pm \sqrt{(y_1 - y_2)^2(r^2((x_1 - x_2)^2 + (y_1 - y_2)^2) - (x_2\,y_1 - x_1\,y_2)^2)}}{(x_1 - x_2)^2 + (y_1 - y_2)^2} \quad (10)$$

where x_1, y_1, x_2, and y_2 are the x and y coordinates as given by the two inner layers. Using the radius of the outer semi-circles, it computes the position of initial hit. Then one only needs the change in the z position, which is easily given by the bar numbers of the semi-circle rods. Additionally, and similar to the 4-layer design, the angular resolution does not change substantially with incoming muon angle (± 1 degree).

The second detector design showed that decreasing the distance between the inner layers allowed more extreme angles to cause coincidence. This, in principle, will increase the flux seen by the detector.

Subterranean Background

Once the detector is deployed in the borehole, it will need to be able to discriminate the subterranean background from the cosmic muons. The subterranean background will include alphas, betas, and gamma rays at various energies. Basic calculations show that the range of alpha particles is insufficient to penetrate the approximately 8 mm thick steel encasing. It was shown in a simulation of beta particles with energies up to 10 MeV that they will also be stopped completely, as 0% of the betas made it through the steel encasing. The gamma rays, however, are able to penetrate through the steel encasing and cause events in the scintillating rods of the detector. Thus, a detailed simulation of the gamma ray sources present underground was performed to determine the percent of gammas making it through the pipe and triggering events in the detector. Known gamma ray sources in the subterranean include ^{40}K, ^{235}U, ^{238}U, and ^{232}Th. The spectrums generated by these isotopes were modeled and used as the gamma ray source used in the simulation. Figure 3.19 shows the histogram obtained when these four sources are

combined to form the total subterranean gamma ray source used. Because the actual activity of the subterranean source is unknown until deployment, gamma ray triggering events are represented in fractional amounts. The simulation ran $4x10^5$ gamma rays following the spectrum in Figure 3.19. Using the postprocessing methods previously described along with an energy threshold, it was found that the background gamma ray events can be completely mitigated using four-fold coincidence and a 200 keV threshold in the detector. Table 3.5 shows the results of the simulation when it is processed at four-fold coincidence with varying threshold levels. The energy threshold is applied to each bar individually, so if a layer is struck with a gamma ray, it must deposit at least the threshold amount or greater in any bar in order to be registered as a hit. The number of gamma rays that cause a four-fold coincidence without any threshold is only 0.12%. As the threshold increases the percentage steadily drops, and eventually at 200 keV there are 0 four-fold gamma ray events in the simulation. This simulation showed that it will be possible to eliminate any background events using a simple layer-by-layer threshold on the energy deposited, in conjunction with a four-fold coincidence requirement.

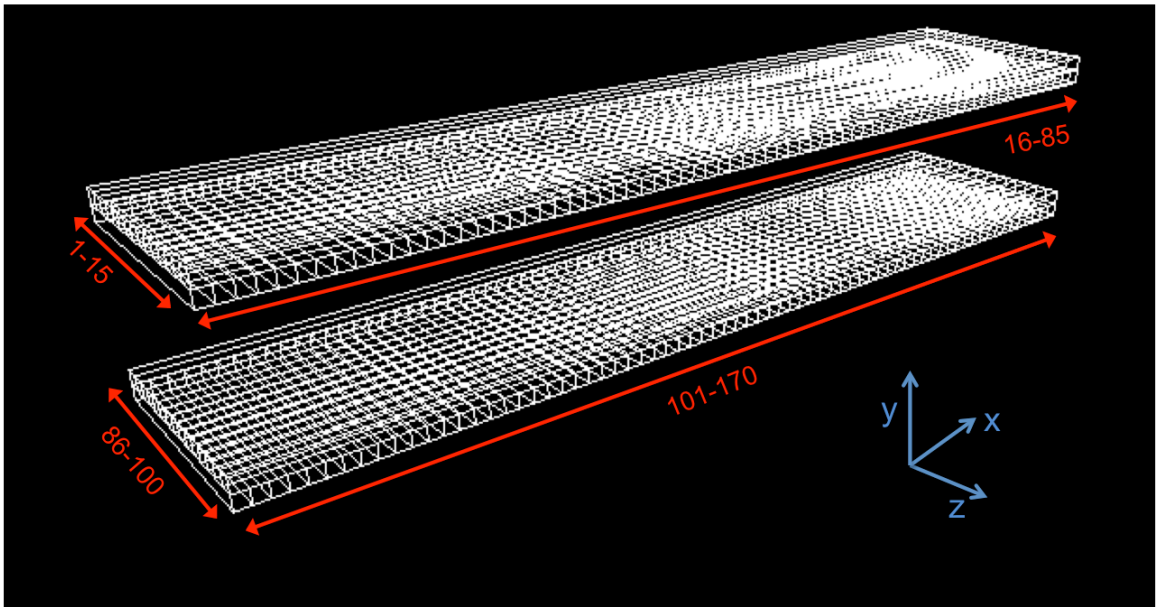

Figure 3.1: Numbering scheme for the rods used throughout the simulations.

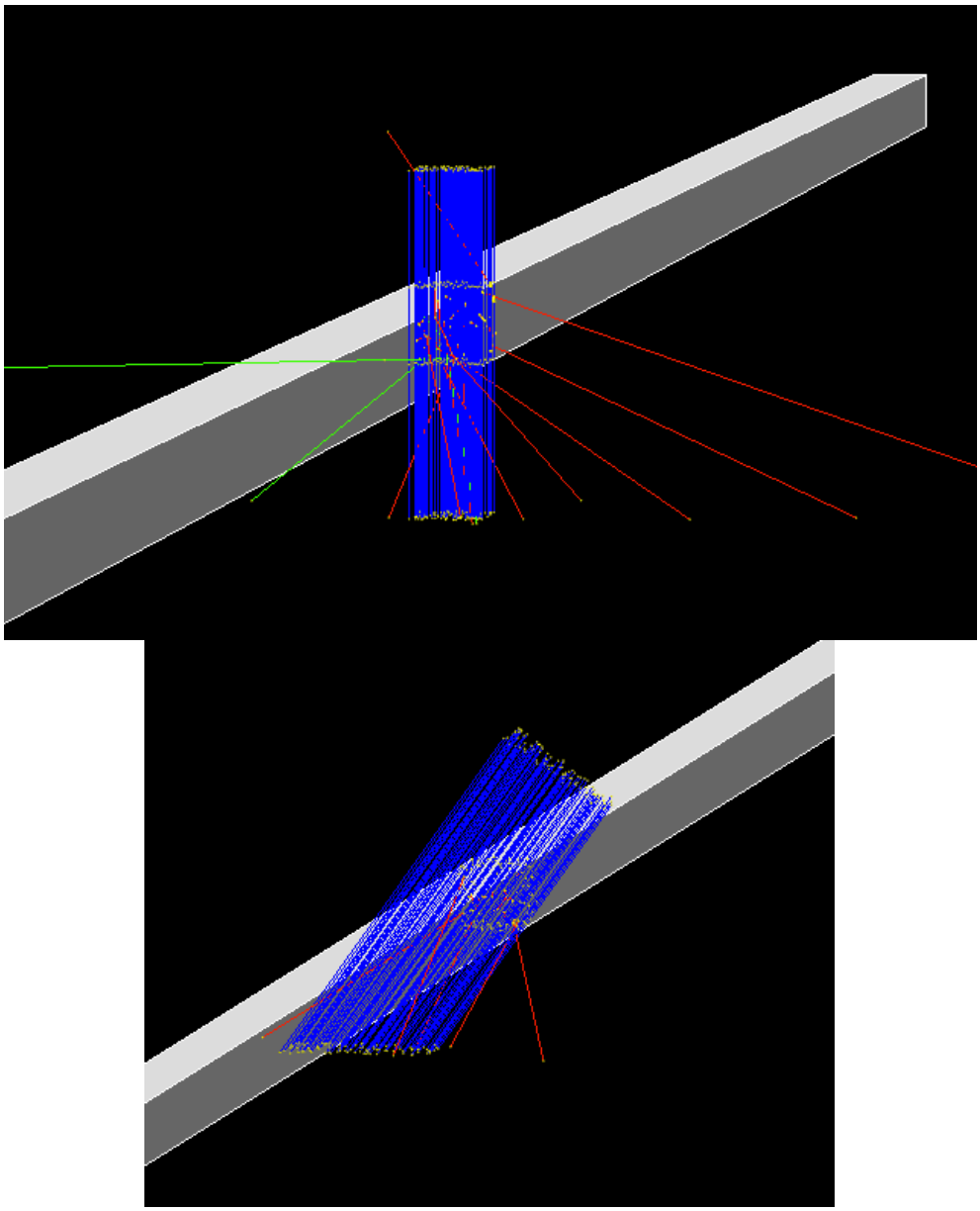

Figure 3.2: Top: Monoenergetic 10 GeV mu+ beam incident on a single polystyrene rod. Bottom: Monoenergetic 10 GeV mu+ beam at 45 degrees from vertical on a single polystyrene rod. Simulation ran 10^5 particles.

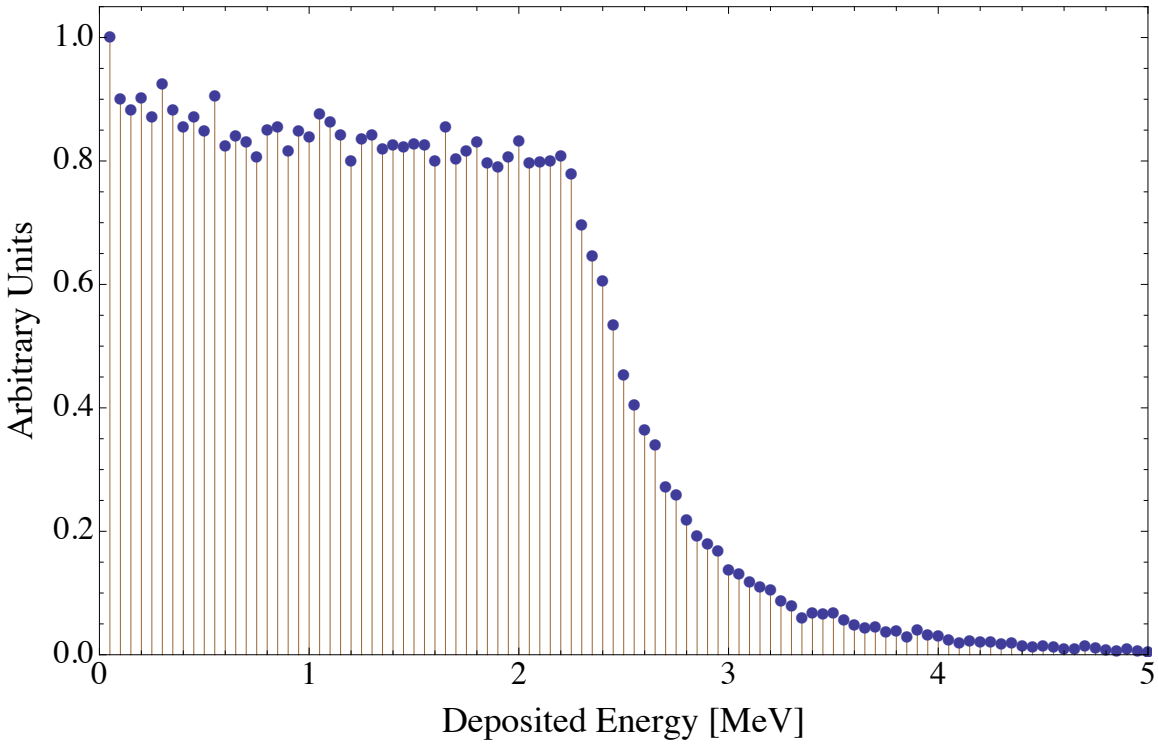

Figure 3.3: Histogram of energy deposition from a 45 degree tilted mu+ source (4 GeV), with a simulation uncertainty of less than 7 keV.

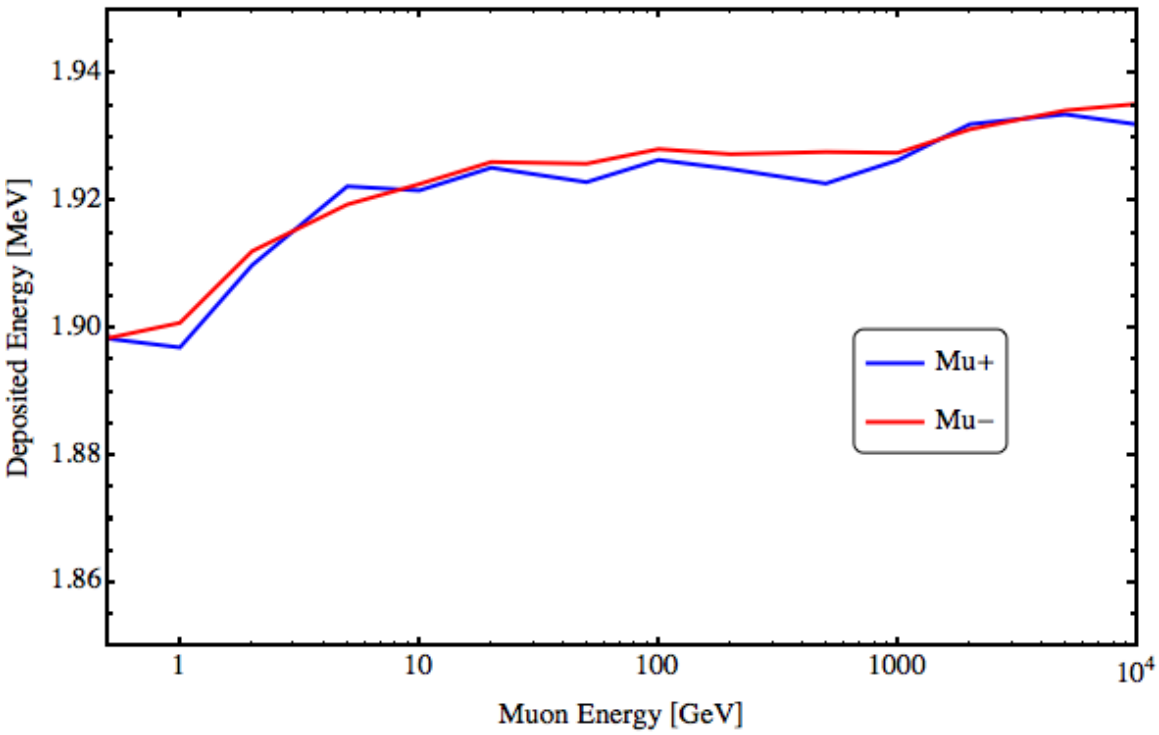

Figure 3.4: Energy deposition in a single polystyrene bar from vertical muons as a function of muon energy. Simulations were run with 10^5 particles.

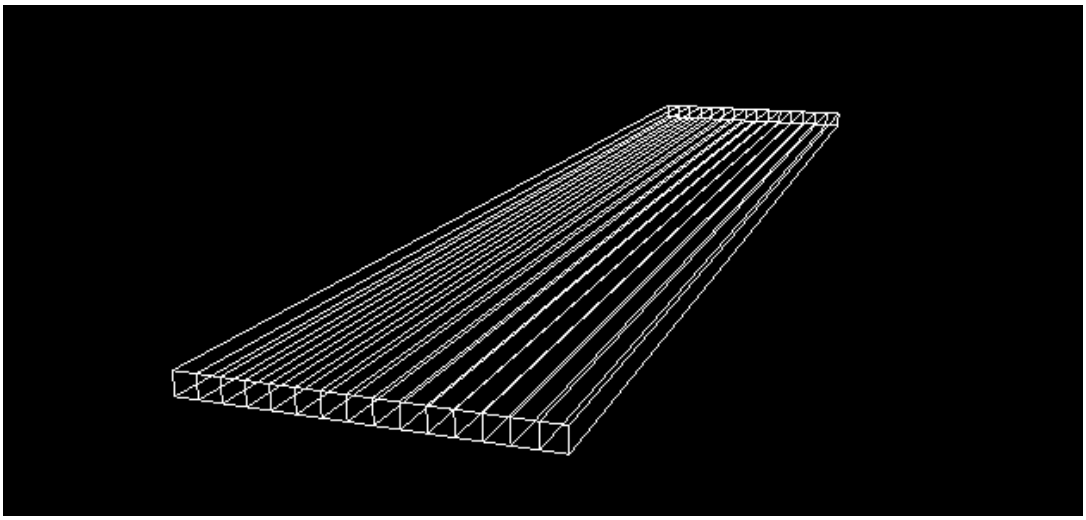

Figure 3.5: Single layer of detector 1 x 15 70 cm long scintillation rods.

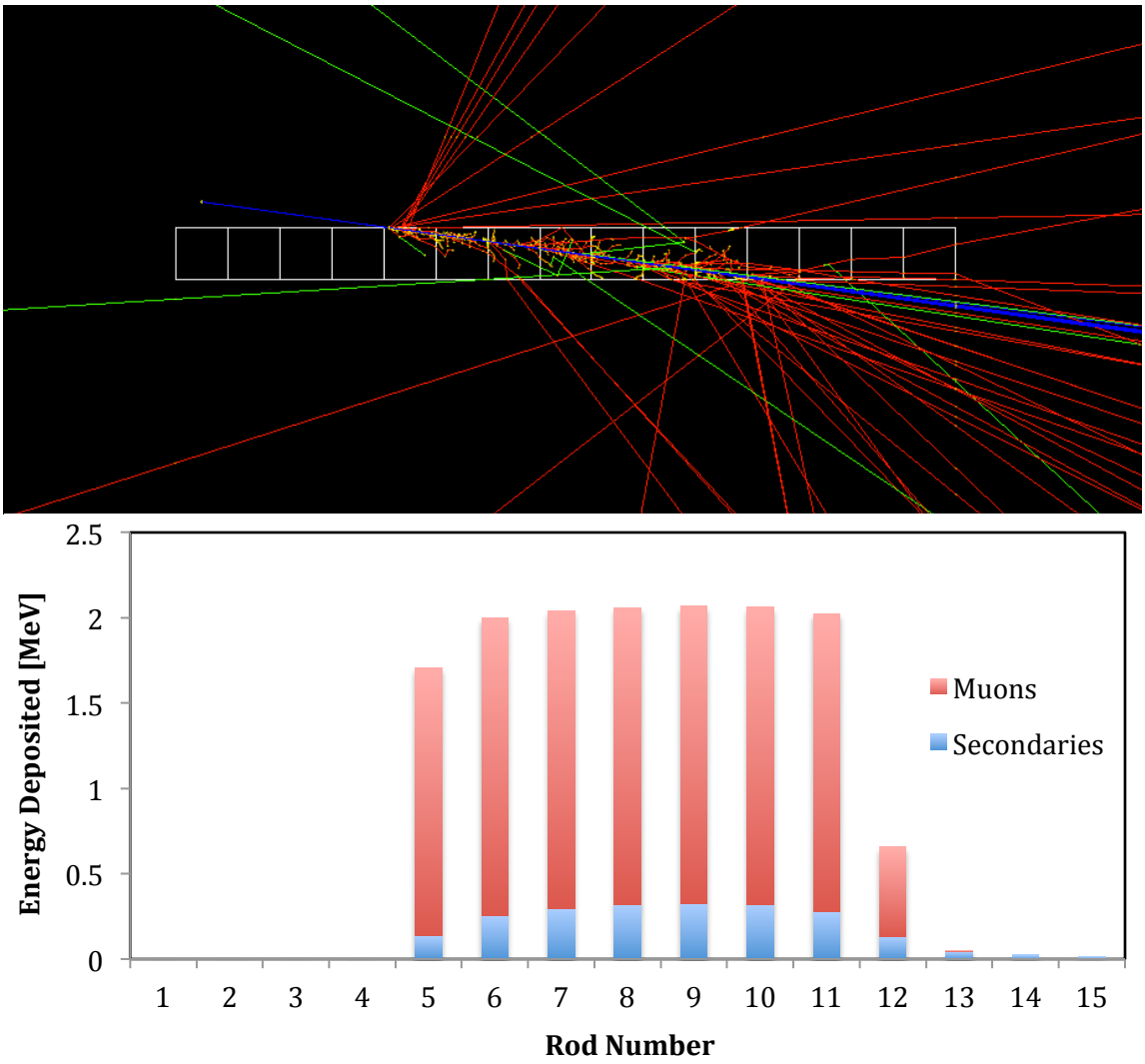

Figure 3.6: Highly tilted (~82 degrees) mu+ beam passing through bars 5-11. The relative contributions of the muons and secondaries to energy deposition in individual bars are shown. Simulation of 10^5 muons. Blue is positive (muons), red is negative (electrons), and green is neutral (gamma rays).

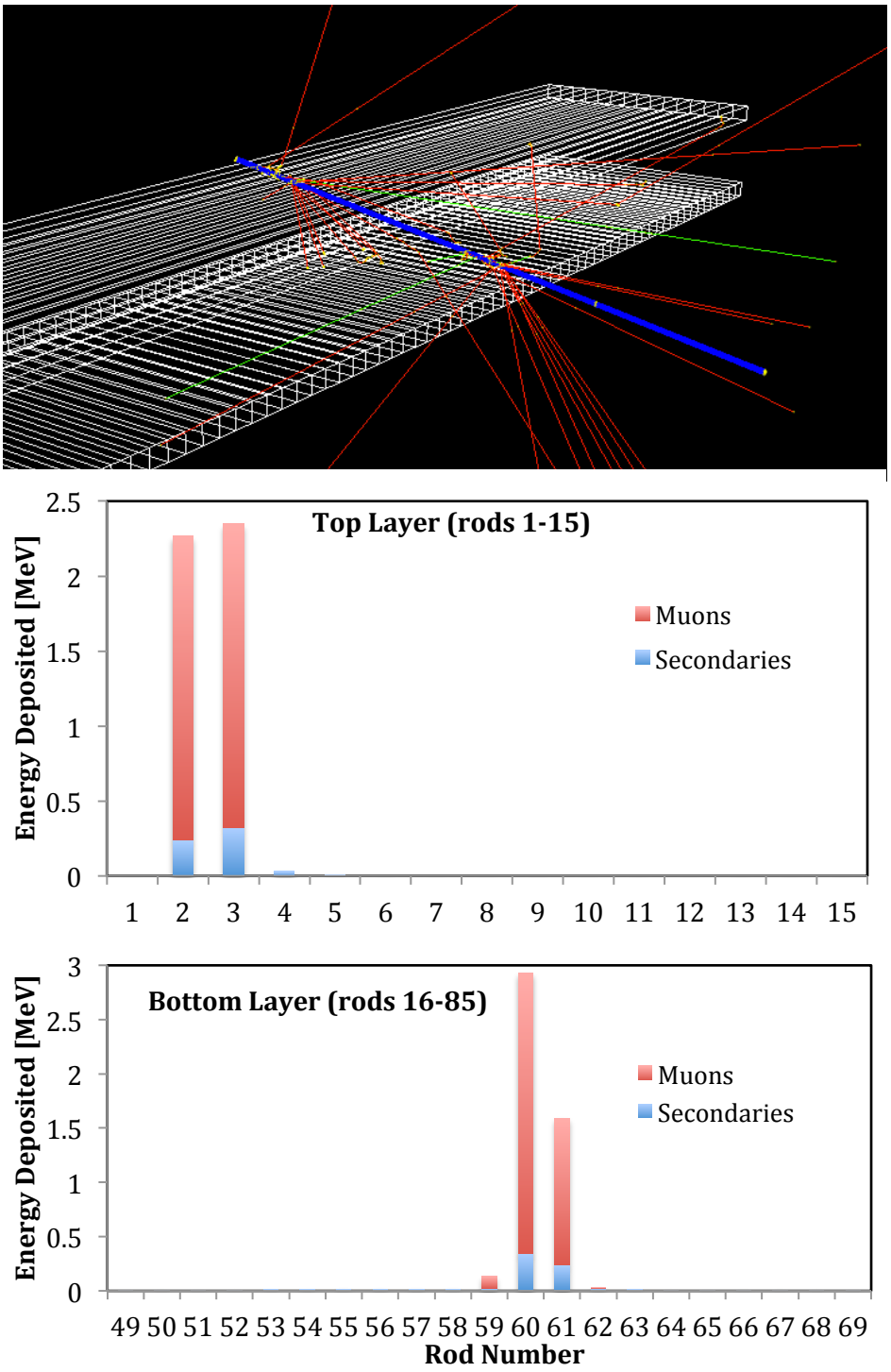

Figure 3.7: Two layer simulation with a 4 GeV mu+ beam at a slant through both layers. Plots show the energy deposition and contribution of muons and secondary particles. There are 5 cm between the layers. Simulation ran 10^5 muons.

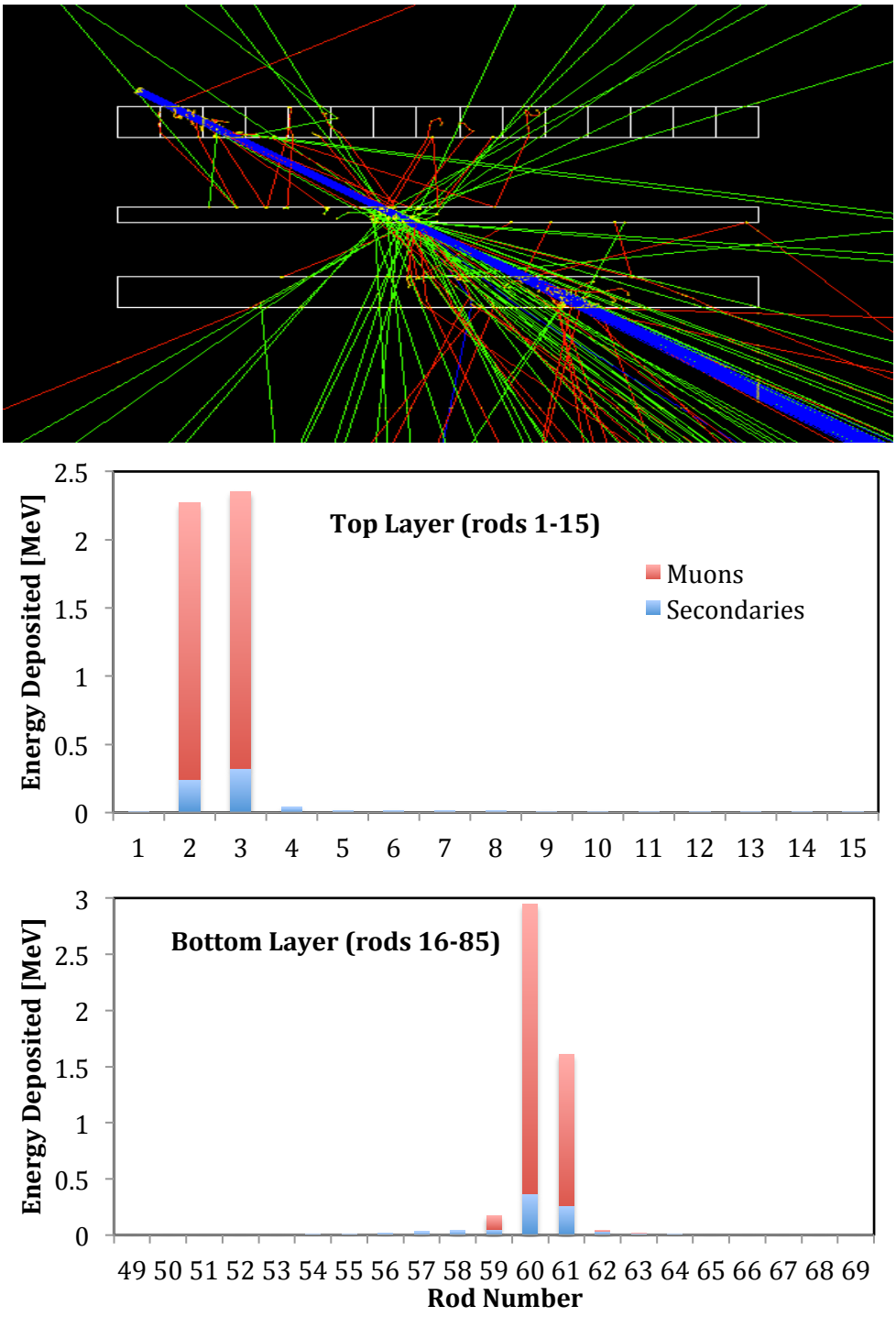

Figure 3.8: Two layer simulation with shielding with a 4 GeV mu+ beam at a slant through both layers. Plots show the energy deposition and contribution of muons and secondary particles. There are 5 cm between the layers. Simulation ran 10^5 muons.

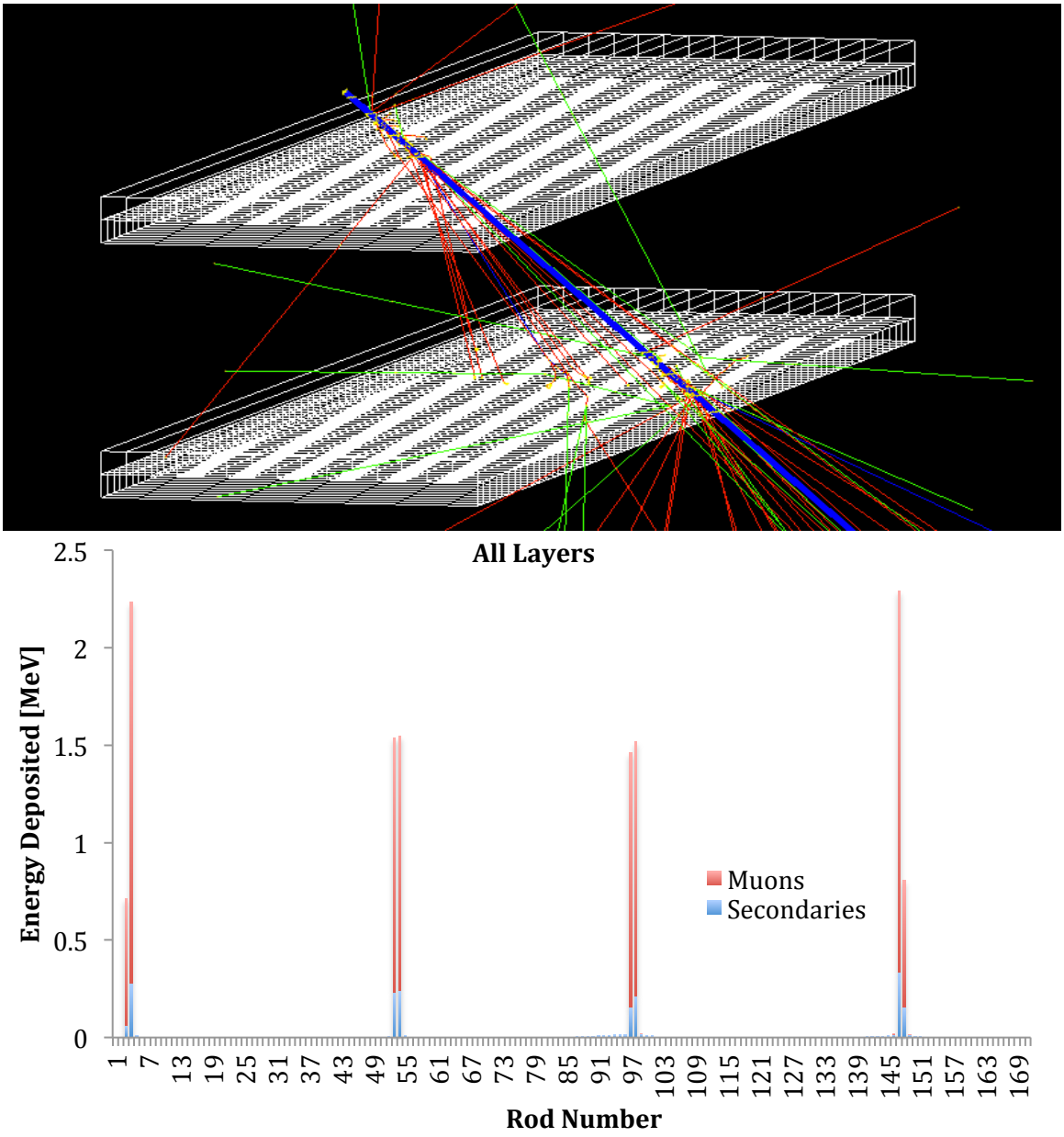

Figure 3.9: Top: Screen shot of Geant4 simulation of full 4-layer detector. Bottom: Energy deposition from a tilted 4 GeV muon beam showing which bars were impacted in each layer, and the relative contributions of muons and secondaries.

Table 3.1: Output from a single simulation event. Time is absolute from beginning of muon movement at source. Time is reset each event. PDG encoding is the particle identification number, 13 is muon, 11 is electron, and negative is the antiparticle equivalent. The end of each event is signified by -100000 (arbitrary number, could be any symbol), placed in the same row as the muon momentum vector.

Energy Deposited [MeV]	Rod #	Time [ns]	PDG Encoding
1.03274	2	0.0670011	-13
1.64999	3	0.0992387	-13
1.23682	52	0.124284	-13
1.13627	53	0.149682	-13
1.44401	96	0.633641	-13
0.993576	97	0.654442	-13
1.32002	146	0.681332	-13
0.372838	146	0.689731	-13
0.896579	147	0.704928	-13
0.0600838	146	0.682581	11
0.21081	146	0.683792	11
0.23678	146	0.685336	11
2174.51	-2718.14	2174.51	-100000

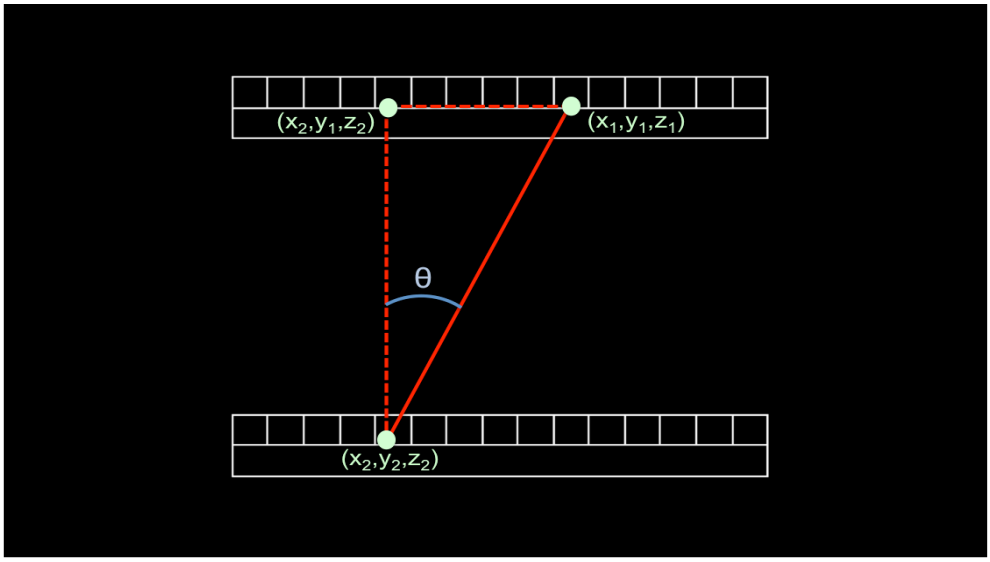

Figure 3.10: Trigonometry used to compute zenith angle.

Table 3.2: Example calculation using the event shown in Table 3.1 of the maximum and average methods of determining hit location.

Energy Deposited [MeV]	Rod #	Calculated Location	
		Maximum	Average
1.03274	2	3	2.62
1.64999	3		
1.23682	52	52	52.48
1.13627	53		
1.44401	96	96	96.41
0.993576	97		
1.32002	146	146	146.29
0.372838	146		
0.896579	147		
0.0600838	146		
0.21081	146		
0.23678	146		

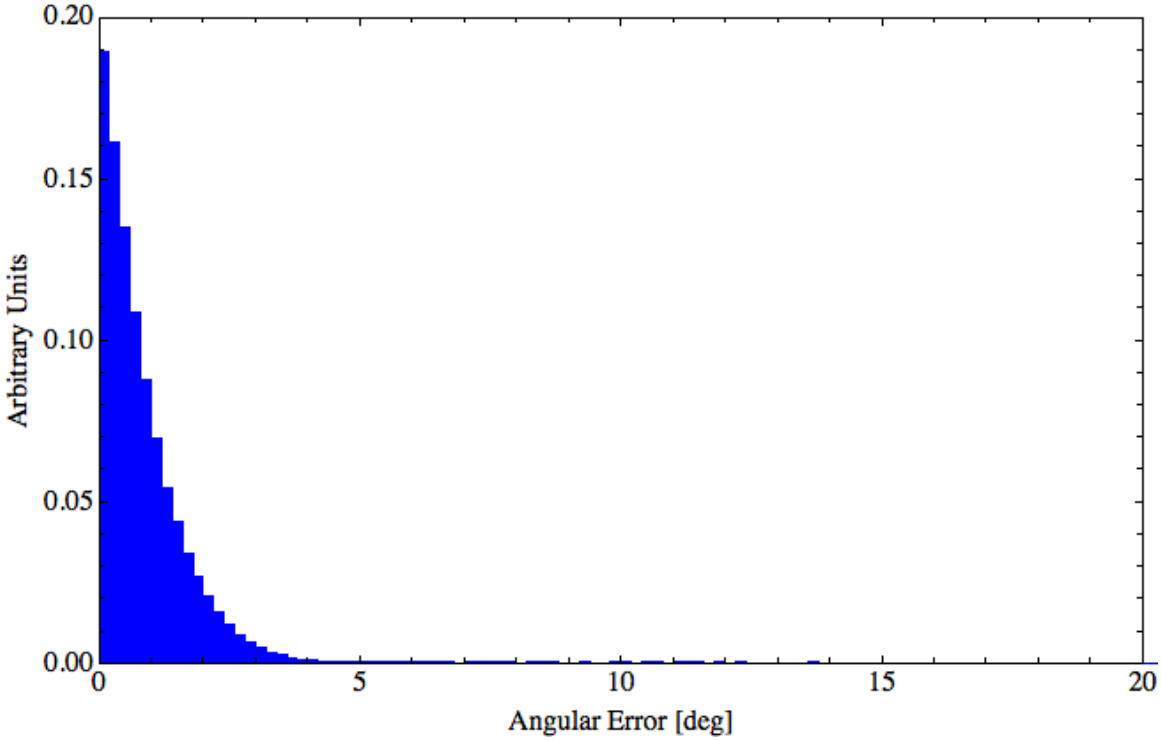

Figure 3.11: Probability mass function of angular error with the detector at 11 centimeter spacing between inner layers. Maximum error was 65.2 degrees, with a mean and a median of 0.97 and 0.62 degrees, respectively. Only 1.2% of events have an error greater than 5 degrees.

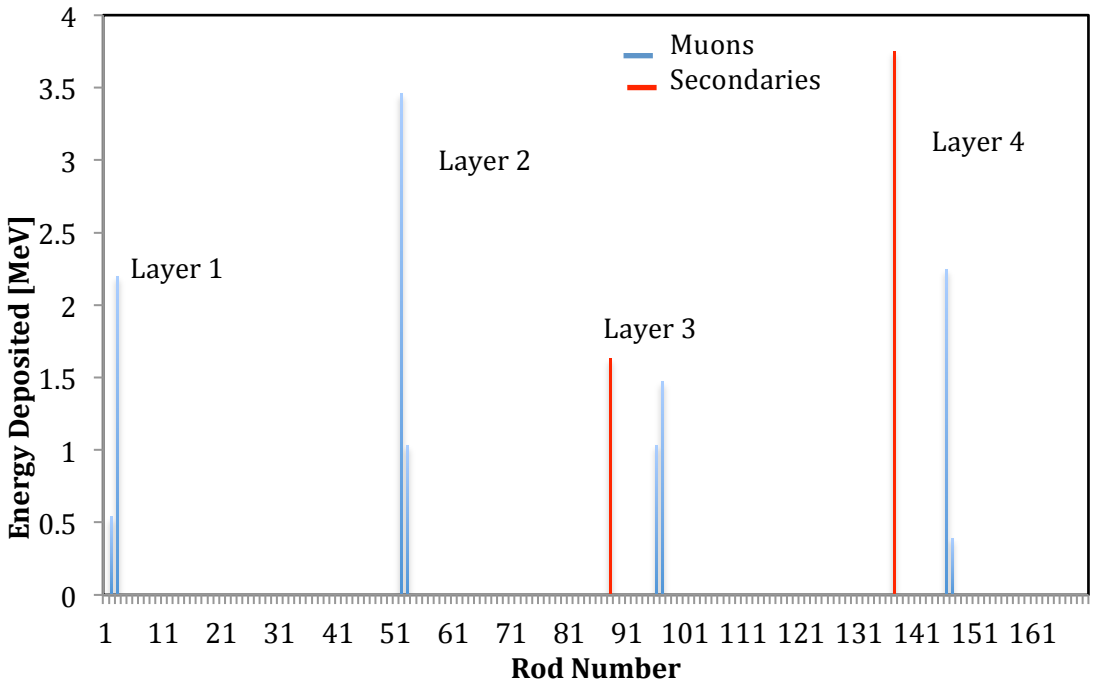

Figure 3.12: Plot showing an event that produced an error of 48 degrees. There were approximately 35 individual hits. Red is for electron deposits while blue is muon. No gammas were produced in this event, and no shielding was used. Layer 3 and layer 4 had secondary events that deposited more energy than the primary muon events.

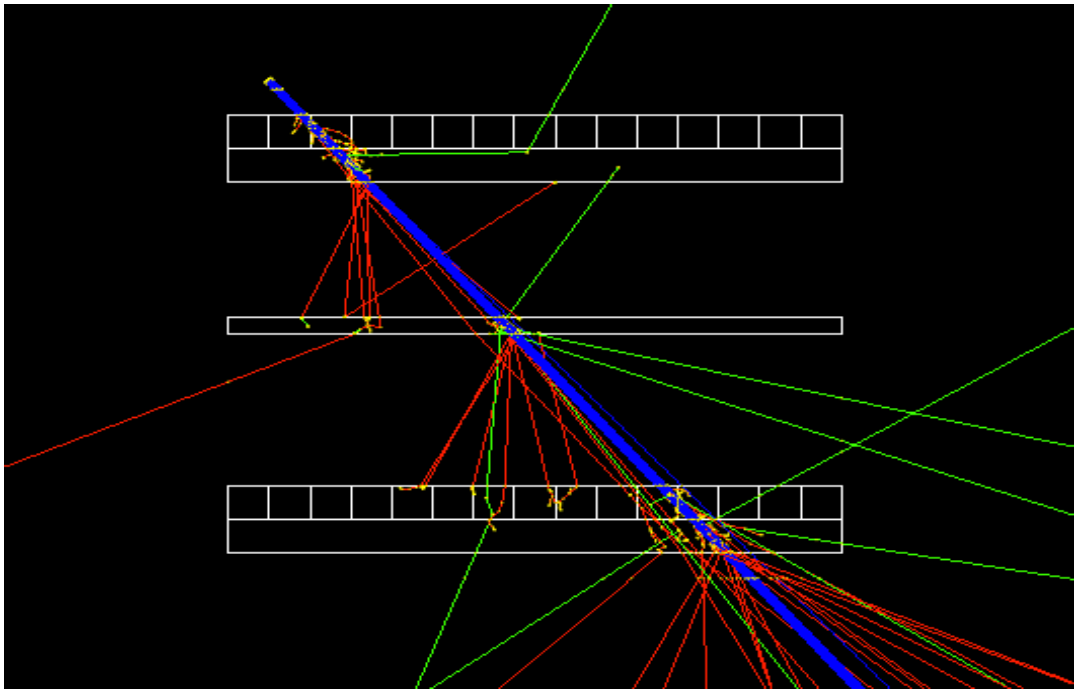

Figure 3.13: Shielding material comparisons and their relative effects on the angular error. The table is organized to show the mean, median, and maximum errors of the simulations. Simulation used 11 cm spacing between layers.

Table 3.3: Mean, median, and max angular error incurred using no shield and shields made of lead, iron, and aluminum.

Angular error	No Shield	Lead	Iron	Aluminum
Mean	0.46	0.5	0.5	0.45
Median	0.21	0.24	0.22	0.21
Max	46	46.5	45.6	46.1

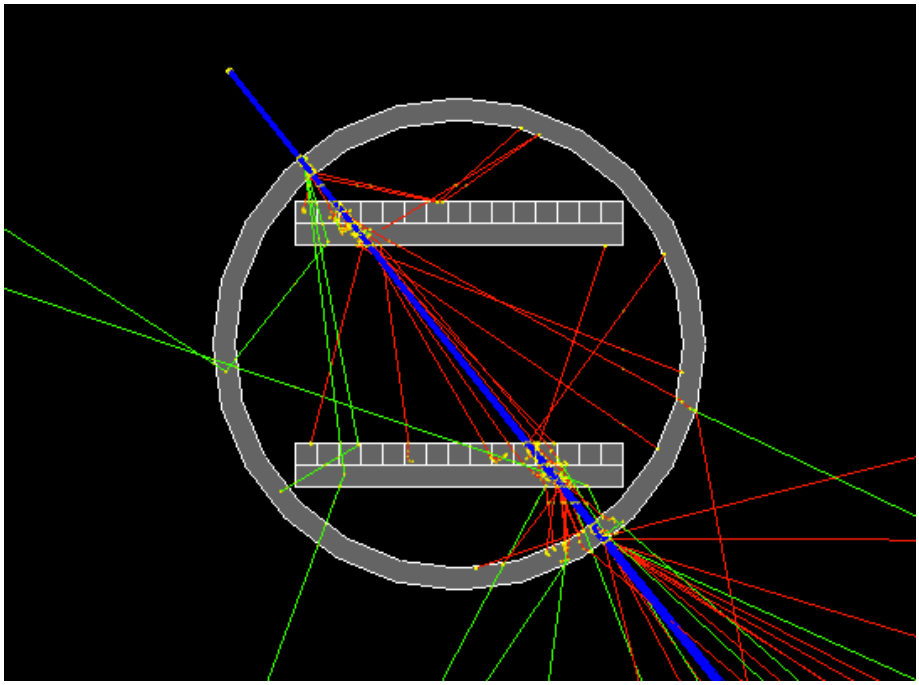

Figure 3.14: Four layer detector with the surrounding stainless steel encasing.

Table 3.4: Effect on detector angular resolution from underground encasing. Simulation was run with 10^5 particles.

		Error (degrees)	
	Angle	Mean	Median
Pipe	90	1.67	0.75
No Pipe	90	1.19	0.69
Pipe	45	1.93	0.69
No Pipe	45	1.17	0.62
Pipe	15	2.98	0.6
No Pipe	15	1.43	0.53

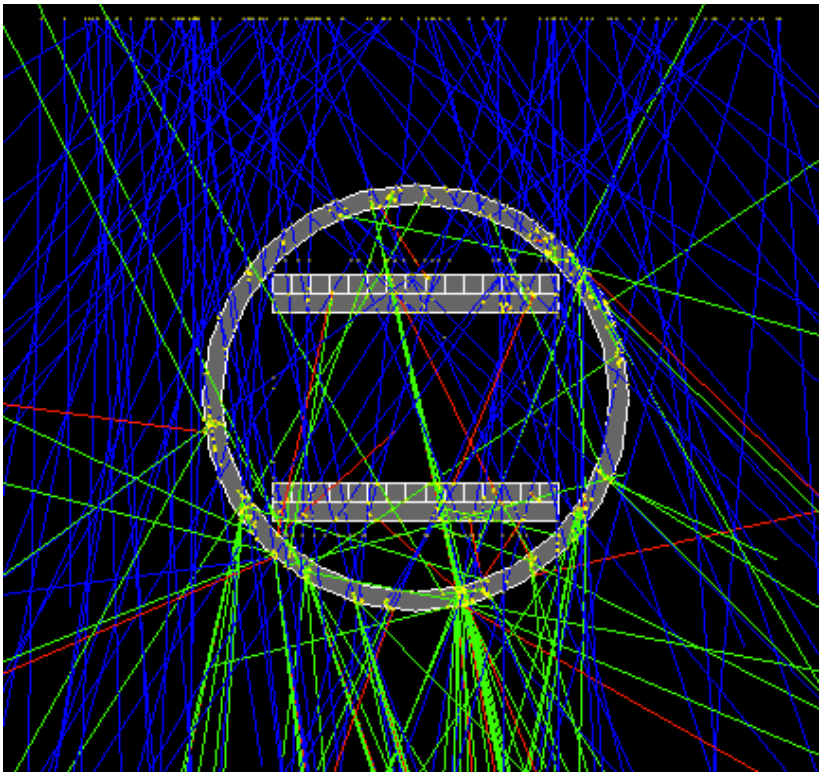

Figure 3.15: Muon spectra at 1500 meters water equivalent. As before, blue are muons, red are electrons, and green are gamma rays or other neutral particles.

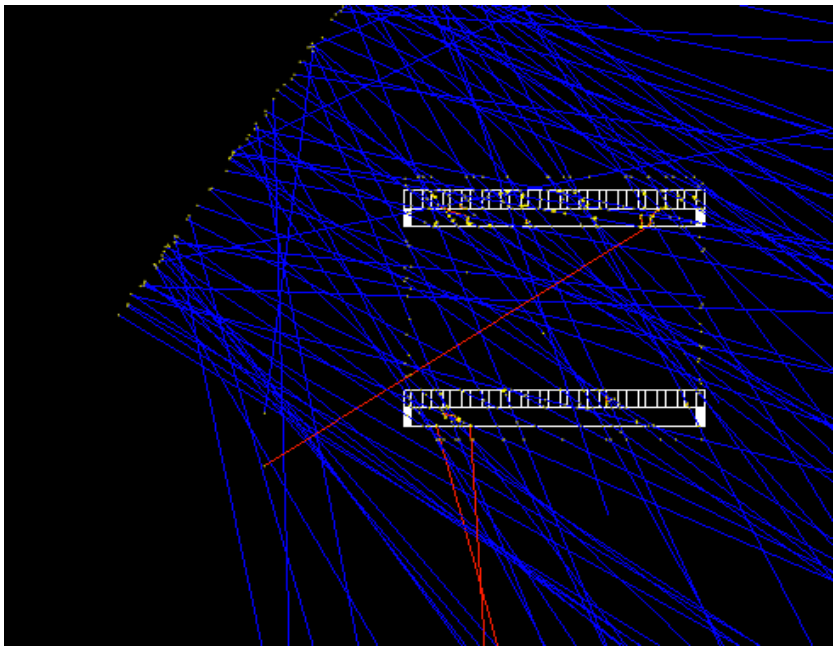

Figure 3.16: Tilted muon source incident on the 4-layer detector. The planar muon source was tilted to determine changes in detector accuracy.

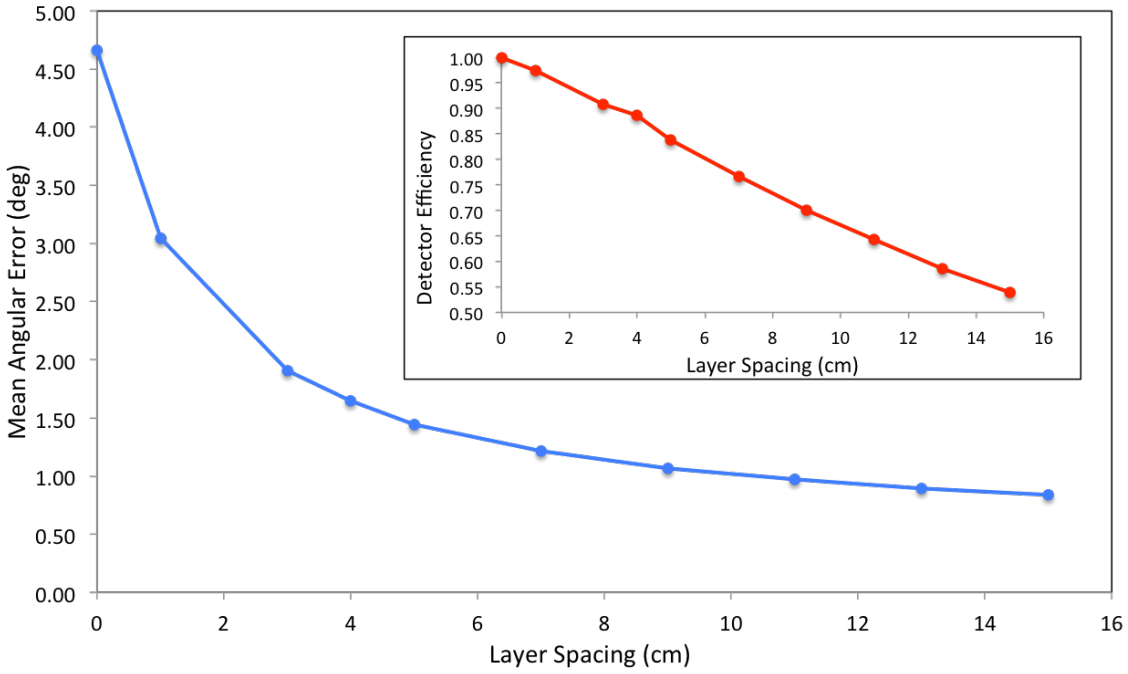

Figure 3.17: Mean angular detector error as a function of the spacing between the inner layers. The graph inside shows how the detector efficiency decreases with layer spacing. Simulation consisted of $3*10^5$ particles using a sea-level muon spectrum.

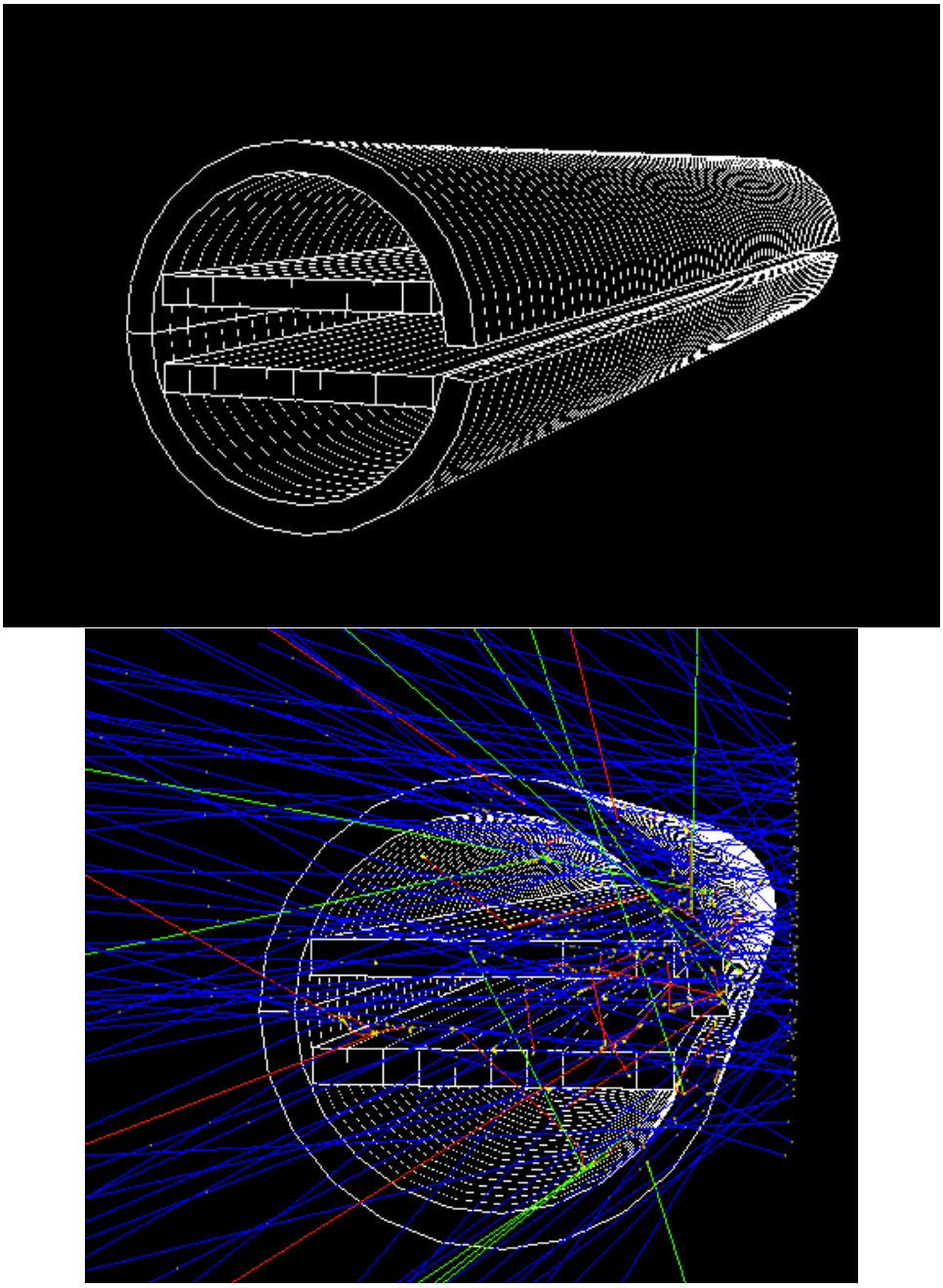

Figure 3.18: Top: Semicircular layered design. The semicircles provide one axis while the two layers provide the second axis for angle computation. Bottom: a 90-degree tilted muon beam interacting with the detector.

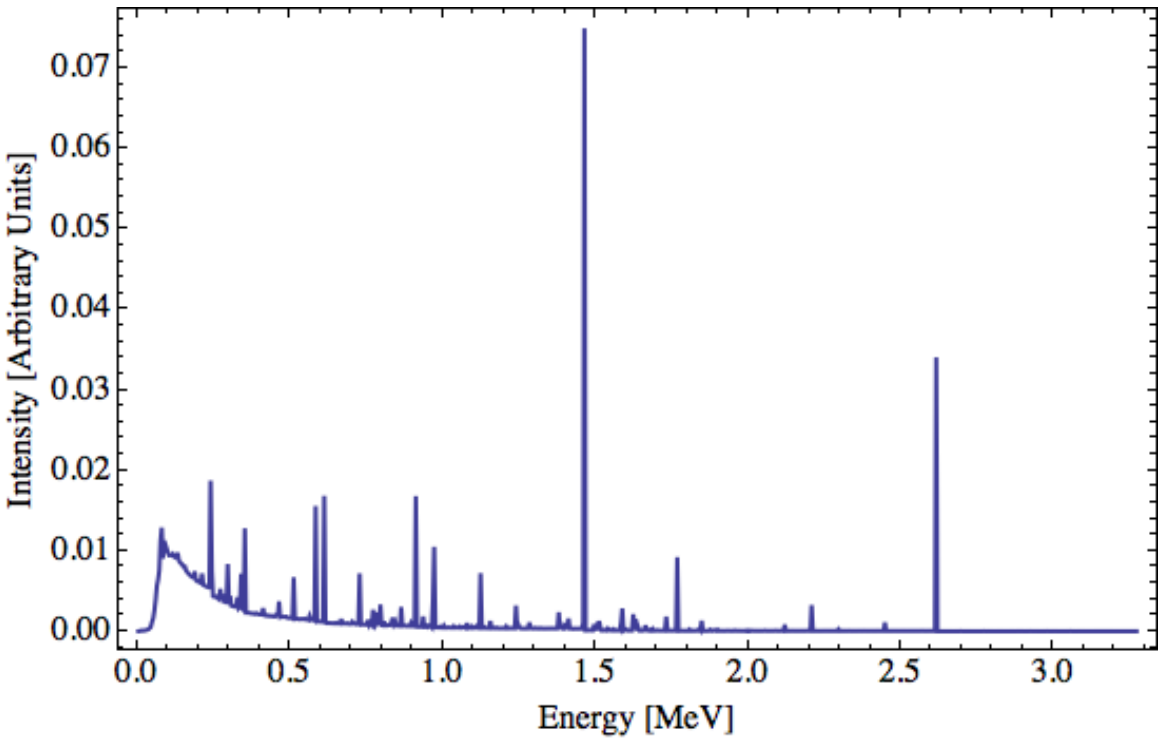

Figure 3.19: Subterranean background spectrum used to model background discrimination in the deployed detector. Gamma ray sources in the subterranean include ^{40}K, ^{235}U, ^{238}U, and ^{232}Th.

Table 3.5 : Various thresholding energies that can be used to reduce gamma ray background interference. Gamma ray loss simulations ran $4x10^5$ particles. The percent incorrect column refers to the expected percent of gamma rays that cause 4-fold coincidence, each time depositing more than the threshold value.

Threshold [MeV]	% Muon Loss	% Incorrect
0	0	0.12
0.025	0.12	0.01
0.05	0.19	4.25E-03
0.10	0.36	1.25E-03
0.15	0.51	2.50E-05
0.20	0.61	0.0
0.30	0.78	0.0
0.40	1.00	0.0
0.50	1.27	0.0

References

Agostinelli, S.; Allison, J.; Amako, K. Geant4-a Simulation Toolkit. *Nucl. Instr. Met. Phys. Res. A* **2003**, *506*, 250–303.

Amako, K.; Guatelli, S.; Ivanchenko, V. N.; Maire, M.; Mascialino, B.; Murakami, K.; Nieminen, P.; Pandola, L.; Parlati, S.; Pia, M. G.; et al. Comparison of Geant4 Electromagnetic Physics Models against the NIST Reference Data. *IEEE Trans. Nucl. Sci.* **2005**, *52* (4), 910–918.

Apostolakis, J.; Bagulya, A.; Elles, S.; Ivanchenko, V. N.; Jacquemier, J.; Maire, M.; Toshito, T.; Urban, L. Validation and Verification of Geant4 Standard Electromagnetic Physics. *J. of Phys: Conf. Ser*. 2010, p 032044.

Lohmann, W.; Kopp, R.; Voss, R. *Energy Loss of Muons in the Energy Range 1-10000 GeV*; 1985.

Macluc, F.; Grupen, C.; Hashim, N. O.; Luitz, S.; Mailov, A.; Müller, A. S.; Putzer, A.; Sander, H. G.; Schmeling, S.; Schmelling, M.; et al. Muon-Pair Production by Atmospheric Muons in CosmoALEPH. *Phys. Rev. Lett.* **2006**, *96* (2), 1–4.

Mulhauser, F. Precision Muon Lifetime at PSI. In *Nuclear Physics B - Proceedings Supplements*; 2006; Vol. 155, pp 358–360.

Wolfram, S. Mathematica. Wolfram Research: Champaign, IL; 2012.

Yarba, J. Recent Developments and Validation of Geant4 Hadronic Physics. *J. Phys. Conf. Ser.* **2012**, *396* (PART 2).

CHAPTER 4

EXPERIMENTS

Preliminary experiments on the basic components of the detector were performed at Pacific Northwest National Laboratory in Richland, Washington. The goal of the experiments was to optimize the physical design of the first prototype and verify the simulation predictions before a full-scale prototype device was built. The performance parameters tested were the light transport of the scintillating rods, the light transmission with wavelength shifting fibers, as well as the impact of glue to aid the coupling between the fibers and scintillating rods. The scintillating rods used were produced by Fermi National Laboratory in Batavia, Illinois, and are polystyrene rods (Fermilab) doped with POP and POPOP fluours and have a titanium dioxide (TiO_2) coating. The TiO_2 coating is put on as part of the rod extrusion process, making it robust. The coating also serves an important purpose of mitigating light sharing between the rods and increasing internal reflection. The fibers used were wavelength shifting (WLS) scintillating BCF-20 fibers made by Saint-Gobain (Saint-Gobain, 2005). They have a polystyrene core and are clad with a reflective coating. They have an emission spectrum that peaks at approximately 490 nm. The glue is BC-600 optical cement made by Saint-Gobain that was tested as a coupling agent between the 2 mm fiber and the 3 mm hole in the polystyrene rod. Figure 4.1 shows a rendering of the basic detector design (as explained in Chapter 1), and shows the many polystyrene rods with the 3 mm holes for the fibers. Figure 4.2 is a picture of the basic experimental setup that included one Hamamatsu photomultiplier tube (PMT), lead shielding, and a light-tight box.

Light Transport through the Rods and Rods with Fibers

The scintillation light produced in the rods as a result of energetic particle interactions will be attenuated as it travels towards the PMT. This will result in a diminished signal. To improve

the light collection efficiency of the rods, it was expected that inserting a fiber into the hole in the middle of the polystyrene rod would help the light transport through the rod because the rod is somewhat self-absorbing to the light emitted from the fluours. To quantify the expected improvement of the light transport through a rod with a fiber inserted several experiments were performed to compare the count rates as a ^{60}Co gamma ray source was moved along a rod, with and without a fiber inserted. Figure 4.3 summarizes the results of this experiment. It is clear from the figure that the fibers greatly decrease light loss as the source is moved further away from the end of the rod. The fiber increases light transmission by approximately 2 orders or magnitude. However, one variable not immediately discerned from Figure 4.3 was that the PMT did not have sufficient applied voltage to produce a signal much higher than background counts. Thus, although this experiment did lead to the correct conclusion, the steep drop off near the beginning followed by a leveling off represented the data approaching background. However, the fact that the fiber leveled off at a much higher background rate means the light transmission is greatly improved using a fiber. Additionally, the steep drop of counts at the beginning of the rod and fiber data could mean the rod was contributing at small lengths without needing the fiber for longer distance transmission, as shown in the plain rod data.

One other confounding factor not initially realized was the effect that gamma rays had directly on the PMT. Gamma rays can directly cause a response in the PMT, producing an increase in counts when the source is near the PMT opening. Figure 4.4 shows the PMT response to direct gamma ray interactions with no scintillator present. As the gamma ray source was moved away from the PMT, the background counts registered dropped predictably. It was clear that the signal obtained in Figure 4.3 was artificially increased at short distances. This problem was easily solved using lead shielding around the PMT, especially over the front window.

The response of the scintillating rod from the ^{60}Co source was simulated in order to better understand the responses seen experimentally. A ^{60}Co source has two gamma ray peaks that are coincident 99.88% of the time. They have energies of 1.17 and 1.33 MeV, with Compton edges at 0.963 and 1.12 MeV, respectively. Figure 4.5 shows the simulated response of the scintillating rods from the ^{60}Co gamma ray. The PMT response to energy deposited at locations along the rod

is directly proportional to the number of photons that reach the PMT. The energy deposited experimentally from the gamma rays is due to the Compton energy distribution, which resulted in the long tail seen towards 0 MeV in Figure 4.5. It is clear that the number of counts decreases as the energy deposited exceeds about 1 MeV. The signal "smearing" was found to be more significant in the lower energies in lab experiments due to loss of light reaching the PMT, with minor but additional contributions from the electronics and inherent PMT noise.

Several additional experiments were performed to determine the impact of glue between the fiber and the rod. A simple gluing procedure was developed and implemented to ensure no air bubbles were formed in the glue, changing the index of refraction. The rods which had fibers glued in were then tested and the results compared to what was obtained with the rods where the fibers were only inserted with an air gap. The experimental setup for this testing is shown in Figure 4.2. This PS rod was 68 cm long, and the red source shown is the ^{60}Co gamma ray source.

An interesting result was obtained from these experiments, as shown in Figure 4.6. The intent of the experiment was only to determine the impact of gluing the fiber on the light loss rate. Given the relative amounts of signal to background, and the high light loss rate, it was initially difficult to come to any conclusions. After several experiments were inconclusive, the voltage across the PMT was increased from 1980 V to 2180 V. This produced an increase in the count rate, as expected, and overwhelmed the background counts that were previously confounding the data. Also, as the source was moved along the rod at this higher voltage, the response (even of the plain rod) was more consistent, and the count rate did not fall so rapidly with distance. The voltage was then increased a few more times with the results recorded. Figure 4.6 shows four different measurements made (among many others) at differing voltages. The voltages used were 1980, 2180, 2280, and 2380 V (all negative) with each voltage increase corresponding to a higher line on the graph.

The spectrum generated by a single rod is shown in Figure 4.7. This spectrum represents the information contained in a typical data point in Figure 4.6. This particular spectrum was from a gamma ray source placed 4.5" from the end of the rod closest to the PMT.

In total, 434031 counts were obtained in 200 s. In comparison, the background counts were only 248 in the same time (adjusted from an 8 h background run).

About 3 orders of magnitude difference exists between the background and the source-initiated counts, but there was still no clear Compton edge from the spectrum. It is difficult to see the clear peaks from the ^{60}Co gamma ray spectrum given how many low energy counts were picked up by the PMT. However, the smeared spectrum was not unexpected. Scintillating rods are notorious for low resolution and are very difficult, if not impossible, to use for any isotopic determination. Thus, the information the PMT receives will not be used (at the present) for pulse shape discrimination, but the muons will be determined by a total energy deposit and coincidence.

Once it was discovered that an increased voltage across the PMT caused a linearity in the light transport response, as mentioned previously, an experiment was performed to determine the ratio of counts when the ^{60}Co source was placed near the beginning and near the end of the rod. Specifically, it was placed at 6.4 cm and 52.1 cm from the PMT, directly on top of the rod as shown in Figure 4.2. The purpose of this experiment was to determine, using the ratio of counts at various positions, whether there was any benefit to gluing the fiber in the rod. The results are shown in Figures 4.8 and 4.9, which are the count rate ratios at various voltages and the associated background counts, respectively. Typically, the rates at -2380 volts were about 200,000 counts in 100 s. Thus, the measurements shown in Figure 4.8 were essentially unaffected by the background present. Additionally, Figure 4.8 shows that there is no significant difference, nor certainly any advantage, in the use of optical glue as a coupling agent between the fiber and the rod. The glue fared much worse at low voltage, and showed no advantage at higher voltages. To investigate the reason why glue did not improve the light transport, another experiment was conducted, measuring the transmission spectrum of the glue. A sample of optical glue was prepared and a spectrometer was used to determine light transmission. Figure 4.10 shows the results of this experiment, with wavelengths ranging from approximately 275 to 800 nm.

With the glue having a transmission percentage around 85% for the fiber emission wavelength region (Saint-Gobain, 2005), this is clearly not the reason for the lack of advantage of

the glue over normal air. The answer is in the index of refractions between the components. The index of refraction of the outer cladding of the fiber is about 1.49 and the index of refraction of the polystyrene rod is 1.60, and the glue is 1.56. Reflection at a surface occurs when the light is traveling from a higher index of refraction to a lower, causing the light to have a propensity to reflect inward. This makes air a better medium between the fiber and the rod because it has an index of refraction of 1 making the difference between the air and the fiber much larger, causing a higher percentage of light to be reflected. However, the fibers will likely be glued in the first prototype as it will make the unit more robust.

Coincidence Measurements

Multiple coincidence measurements were used to measure the muon sea level spectrum. First, a coincidence measurement involving only two rods was set up as shown in Figure 4.11 in the light-tight box. Two Hamamatsu PMTs were used to read the signals from the rods, and a Nuclear Instrumentation Module (NIM) was used to determine the coincidence. From the NIM was attached a Multichannel Analyzer (MCA) with 256 channels that read out the spectrum obtained by the PMT. Additional shielding was used in this experiment (essentially surrounding the rods and PMTs with lead bricks and/or copper sheets to minimize background). The coincidence measurements, by themselves, should be able to discriminate between nearly all other interacting particles and the muons. It was shown in Chapter 3 in the Subterranean Background Discrimination section that only a very small percentage of gamma ray background is able to cause two-fold coincidence, much less the four-fold coincidence that will be required in the final design. Beta particles were absorbed in one of the two rods without reaching the second, and alpha particles certainly would not be capable of travelling far enough to cause a coincidence. Cosmic neutrons, whose flux is nearly the same as cosmic muons, would also need to scatter twice in the consecutive rods. Additionally, in the final design, this rare occurrence would be discriminated against using a simple energy deposition threshold.

The two-rod coincidence experimental set-up was left running for 16 h, and the resulting spectrum obtained in the PMT is shown in Figure 4.12. Additionally, Figure 4.12 shows the spectrum obtained from a noncoincidence setup from a single bar. It is easy to see that the very

high number of low energy counts smears the rest of the spectrum and makes the muon spectrum indiscernible. The blue data in Figure 4.12 represents the spectrum from the two bar coincidence. The blue data has a much more discernible peak around channel 50. This peak was assumed to be the sea-level muon spectrum. The coincidence was capable of mitigating the signal smearing at lower energies, allowing midrange energies to be highly visible. However, it was not clear at this point if the blue data was indeed the muon spectrum, so another experiment was performed.

This next experiment was set up similarly to the two-rod coincidence, but it used three rods on top and three on bottom. All three rods in each layer were coupled to the same PMT. This configuration produced results that were significantly more clear. Figure 4.13 shows the raw spectrum obtained from this setup after 16 h. Once again the spectrum had a clear peak at approximately channel 50 of the MCA. However, in this case, the experiment produced a spectrum less affected by low energy noise, making the peak more prominent and the lower energies had lower counts as compared with the two-rod experiment. The peak at approximately channel 50 was also higher due to the higher surface area of the three-rod setup, which allowed far more muons to produce a coincidence event. As previously discussed in Chapter 3, the sea-level spectrum has many muons at larger angles, making the wider profile of this setup important for gathering more data.

A sea-level muon spectrum was used to perform a Geant4 simulation to help understand the experimental spectra obtained. A 2 x 3 rod setup was simulated with a full-scale energy and angular muon spectrum at sea level to produce the results shown in Figure 4.14. The spectrum shows a clear peak at approximately 2 MeV. The peak in the simulated results isn't as spread as the experimental results. This is likely due to electronic noise (particularly at low energies) in the experiment. The first four channels of the MCA were immediately cut from the data, as they were obviously entirely noise. Additionally, the NIM used to process the PMT output passed the raw data through a Gaussian filter in the amplifier, causing a broadening of the signal, and thus a widening of the overall experimental energy deposit distribution. It was expected that passing the simulated results through a Gaussian filter would make the spectrums more similar. Also,

MCA channel 50 corresponds to approximately 2 MeV energy deposition in the simulation. Thus, the experimental results were placed on the energy deposition axis with the peak at 2 MeV. Once the simulated data had been passed through a Gaussian filter and the results compared with the experimental spectrum, it was clear that a σ value of approximately 0.8 MeV caused the proper amount of broadening of the simulated spectrum. The results are shown in Figure 4.15, where the red line represents the raw Geant4 spectrum shown in Figure 4.14, green shows the Geant4 data with a Gaussian filter, and the blue line is the experimental spectrum shown in Figure 4.13.

The closeness of the distributions (green and blue lines) gives validity to both the experimental work performed and the simulated results. It also shows that the MCA channels of about 10 and lower had a lot of electronic noise, and are not important to the results. The Gaussian broadened Geant4 spectrum also shows that the shape of the distribution obtained experimentally must have been sea-level muons, causing double coincidence. Additionally, these experiments provided a useful framework for background discrimination, as well as confidence in the simulation results, presented in Chapter 3.

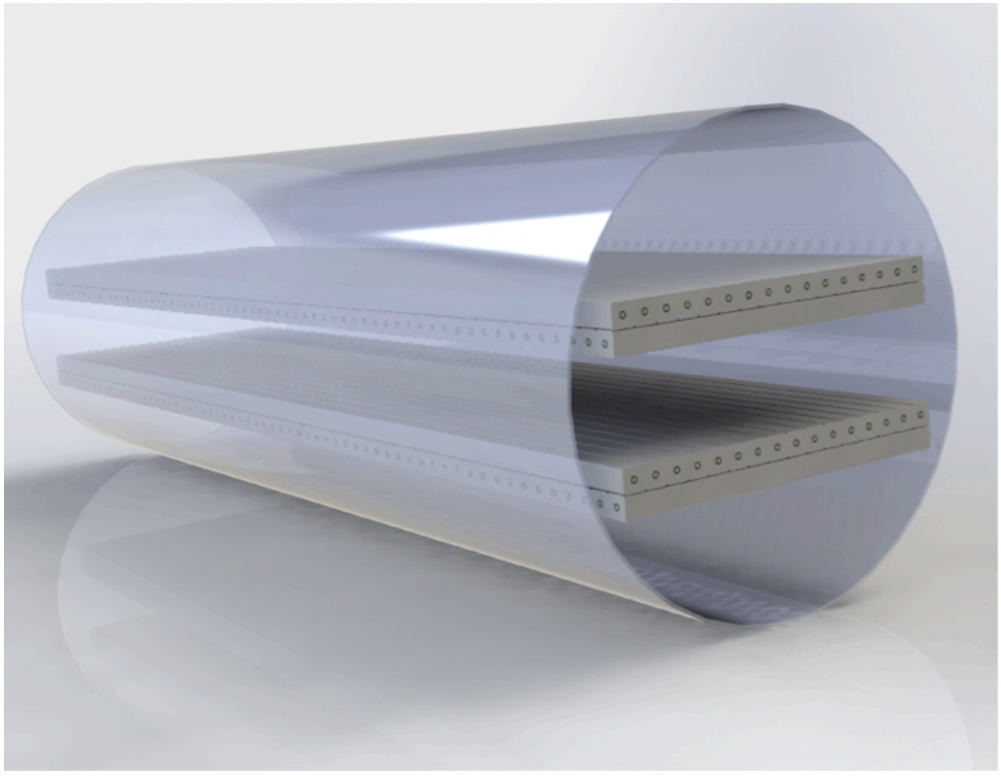

Figure 4.1: Rendering of detector showing the polystyrene rods and the holes for the fibers.

Figure 4.2: Basic experimental setup showing a polystyrene rod with a fiber inserted and a Hamamatsu PMT on one end of the rod to collect emitted light. The gamma ray source was placed at measured lengths from the PMT to determine light transport.

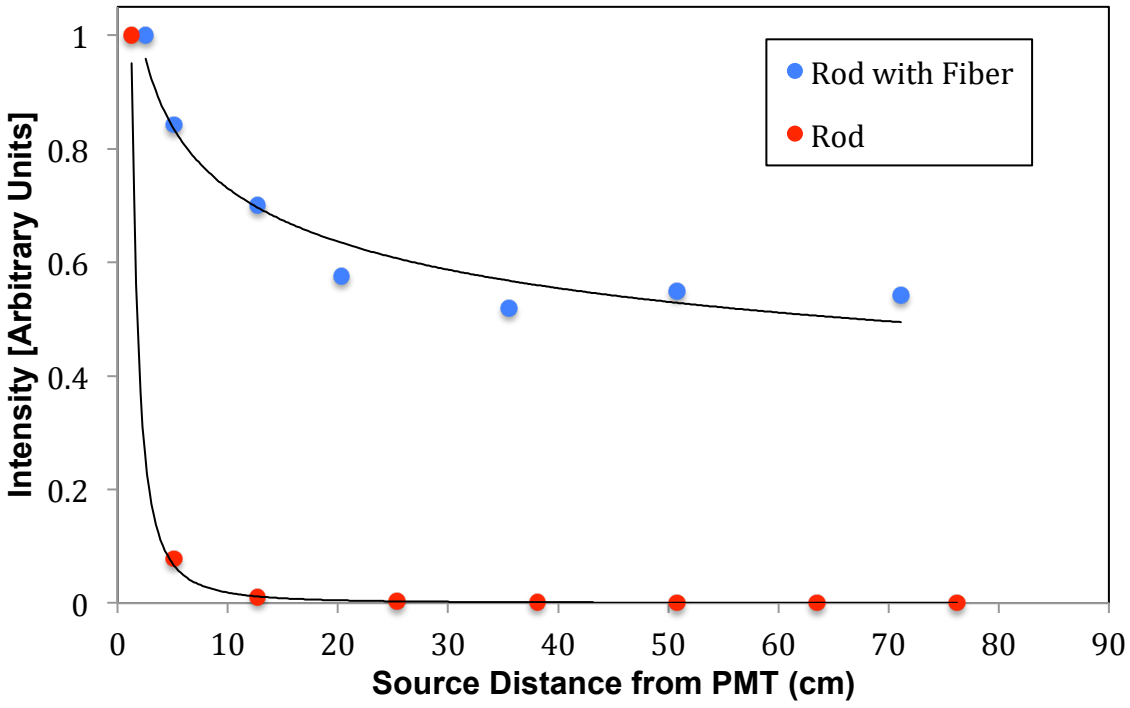

Figure 4.3: Comparison of light transmission between plain rod and a rod with a fiber inserted.

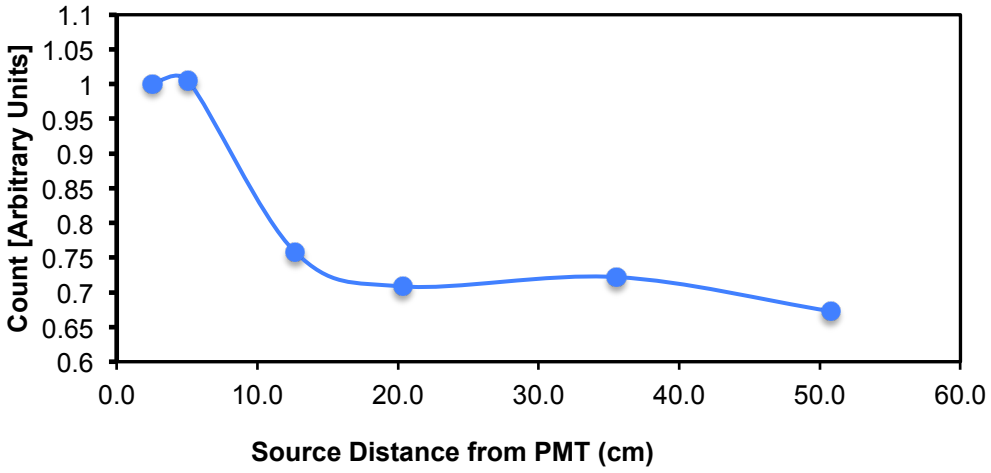

Figure 4.4: Unshielded response of PMT with Co-60 gamma source at varying distances at -1980V.

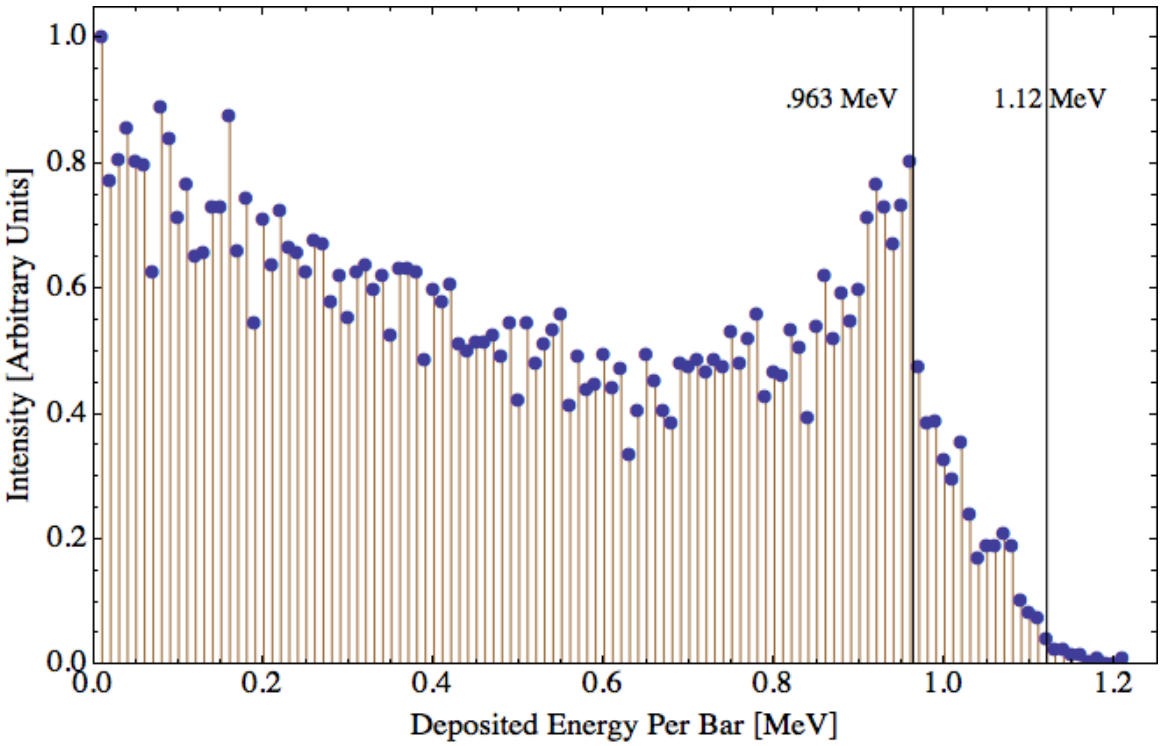

Figure 4.5: Co60 planar source simulation on a single polystyrene rod, showing the intensity normalized occurrence as a function of the energy deposited by each individual gamma ray. The Compton edges are shown on the plot.

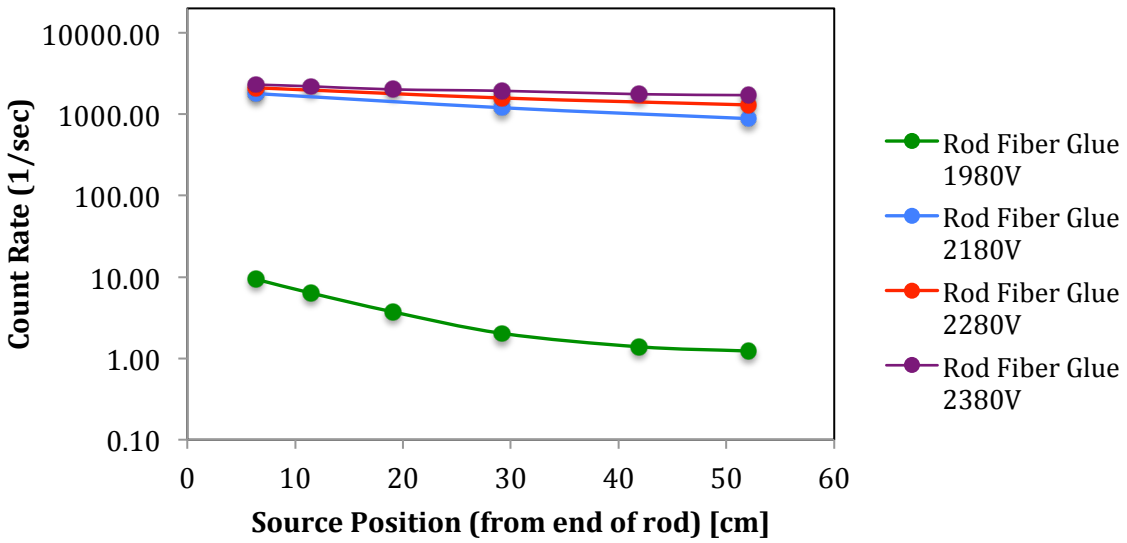

Figure 4.6: The change in count rate and linearity with increased voltage for a fiber glued into a rod are shown. The gamma ray source was placed inside the light tight box.

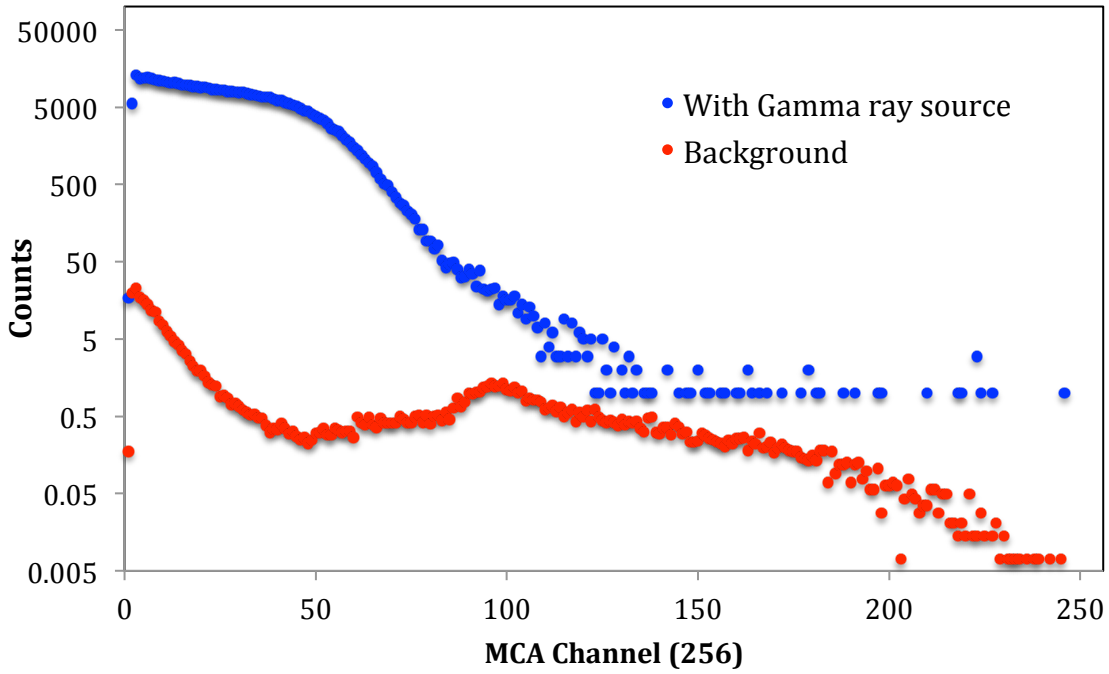

Figure 4.7: The blue data is from a ^{60}Co gamma ray source placed 4.5 inches from the end of the rod. Total counts 434031 in 200 seconds at -1980V. The red data is from background counts adjusted to 200 seconds from 8 hours.

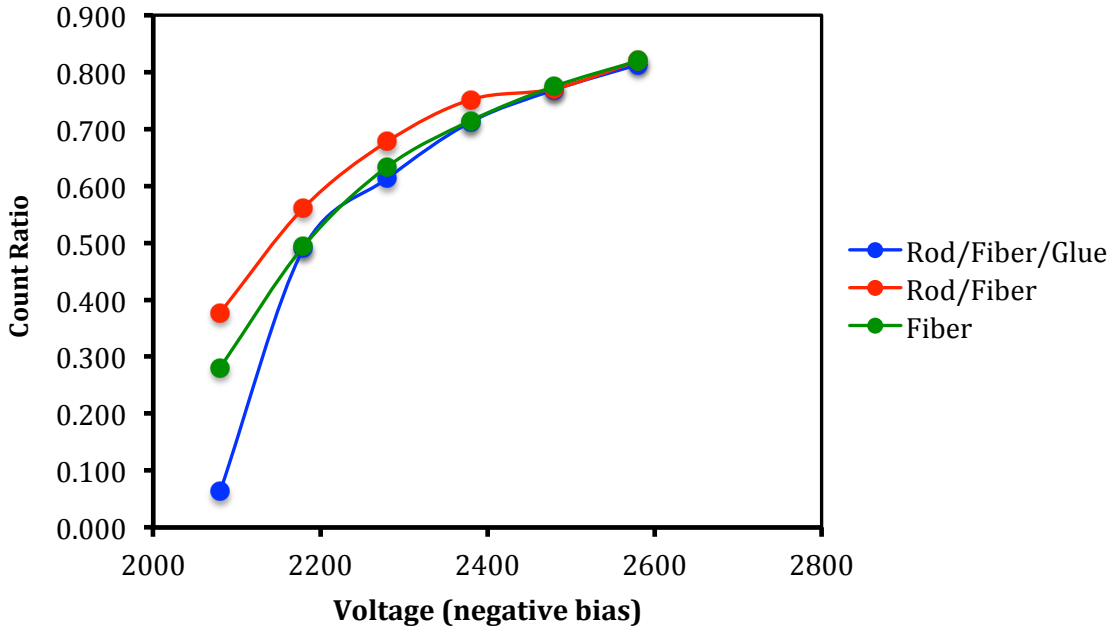

Figure 4.8: Ratio of counts at 6.4 cm and 52.1 cm from the end of the rod as a function of PMT voltage.

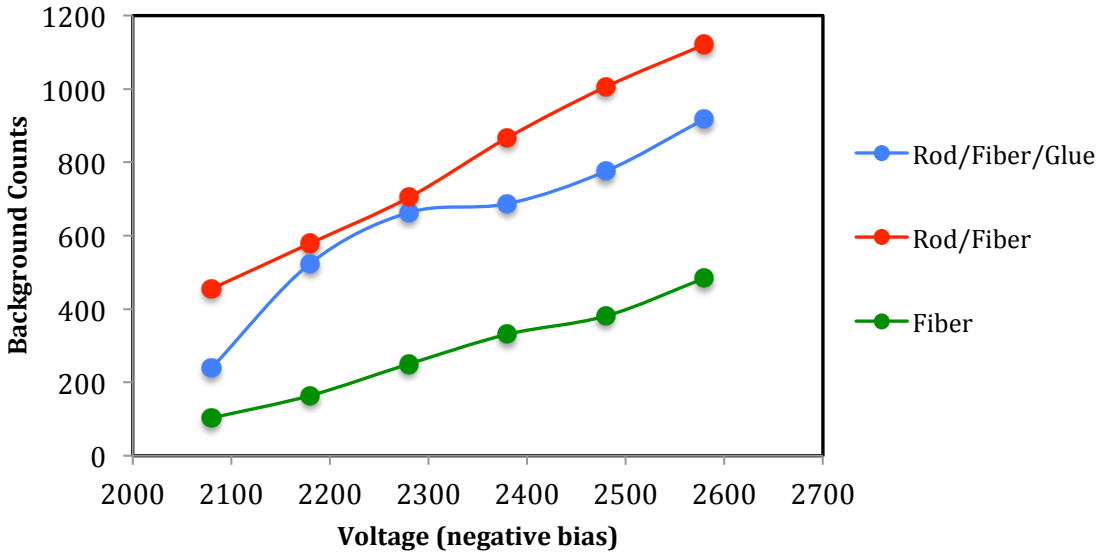

Figure 4.9: Background counts corresponding to the measurements taken in Figure 4.8.

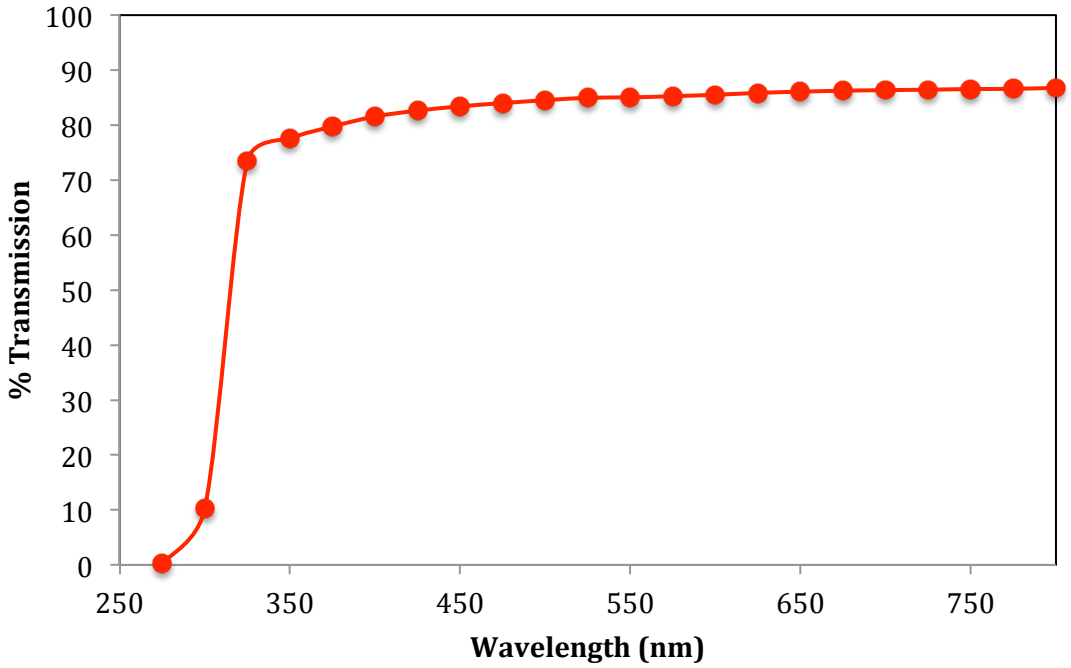

Figure 4.10: Transmission percentage through the optical glue as a function of wavelength.

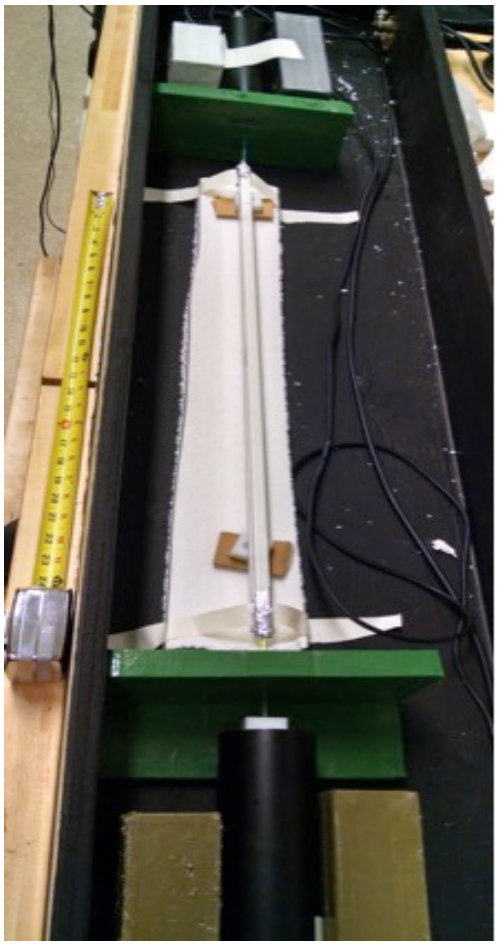

Figure 4.11: Coincidence measurements with two rods (top and bottom orientation). The top rod is connected with the PMT at the bottom of the picture, and the bottom rod to the PMT at the top of the picture. A Nuclear Instrumentation Module (NIM) was used to determine coincidence between the two rods, and a 256 channel Multi-Channel Analyzer (MCA) read out the spectrum obtained from the PMT at the top of the picture.

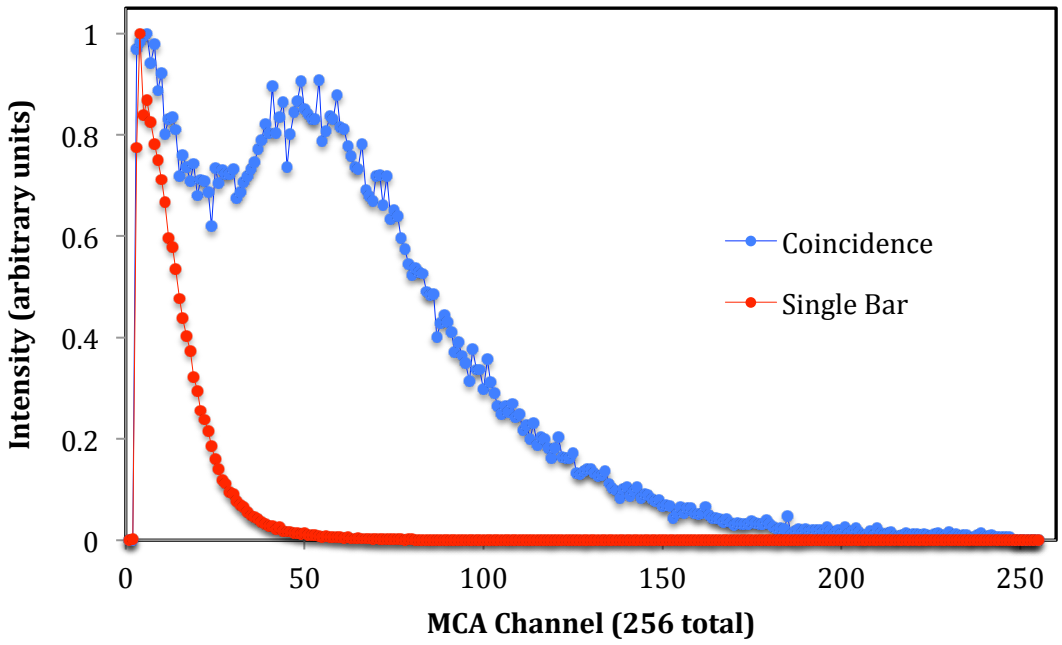

Figure 4.12: Blue shows the background double coincidence spectra after 16 hours using two rods, and the red shows the background spectrum using only a single rod with no coincidence.

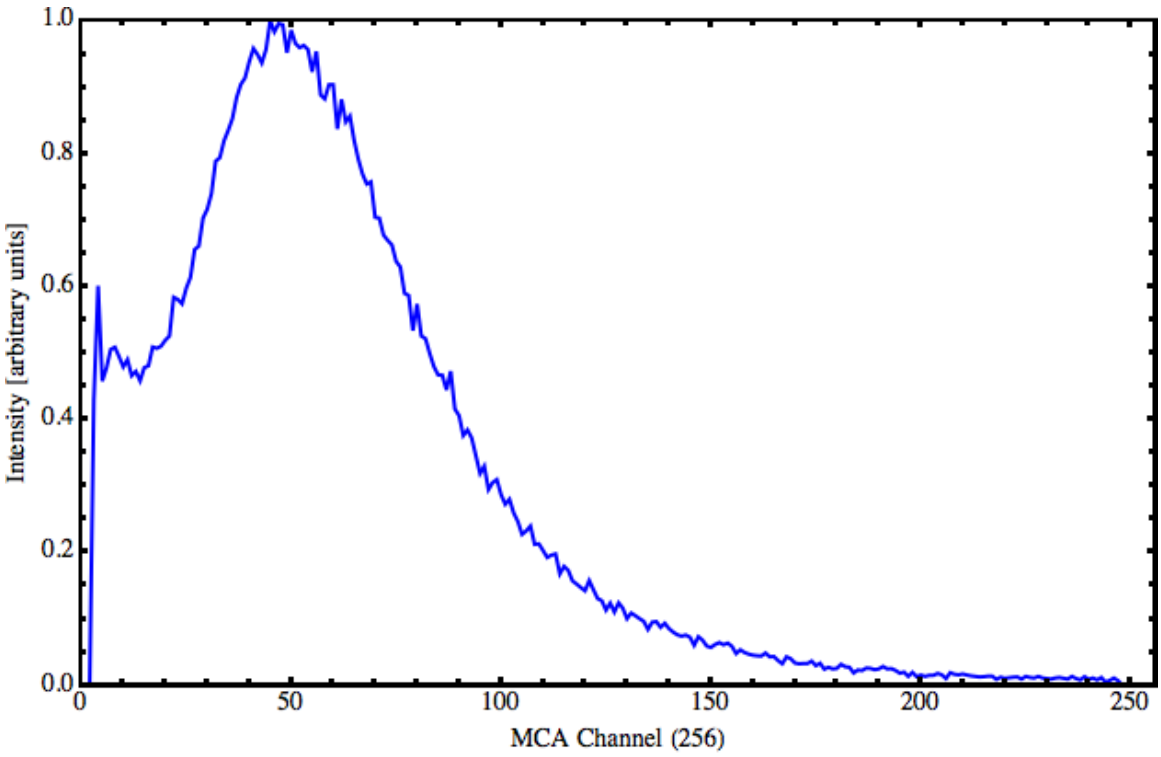

Figure 4.13: Six-rod double coincidence background spectrum after 16 hours.

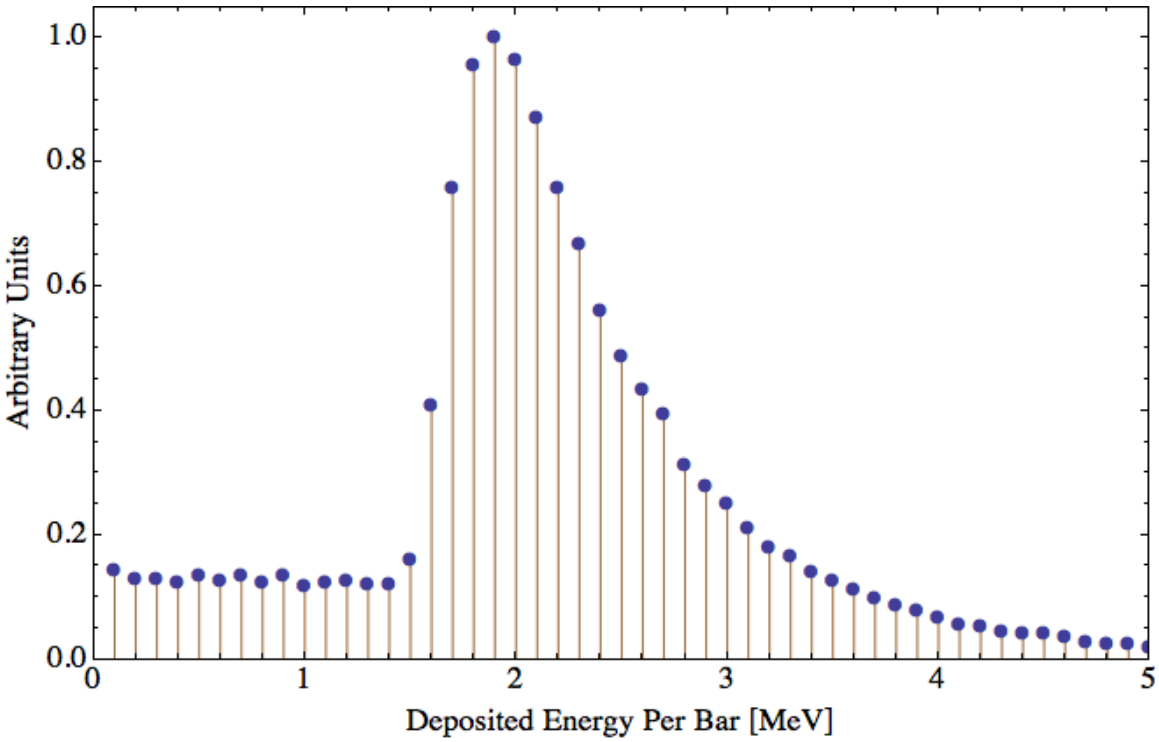

Figure 4.14: Geant4 simulation of a sea level cosmic muon spectrum interacting with a 2 x 3 rod setup. Two layers of three bars each, requiring a coincidence of both layers.

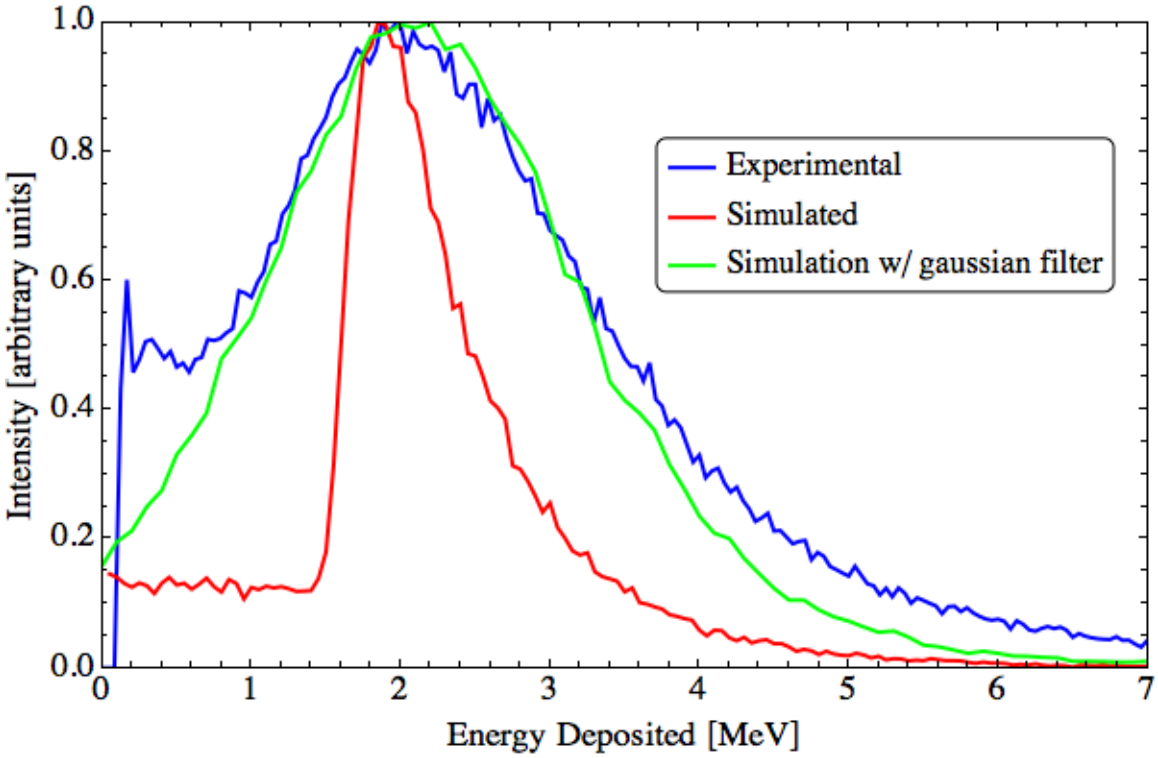

Figure 4.15: Experimental coincidence data with 3 x 2 rod set up. Green - Geant4 simulated energy deposited per muon event. Red - Geant4 simulation results passed through a Gaussian function with a sigma value of 0.8 MeV.

References

Fermilab. Chapter 5 Scintillator Detector Fabrication 5.1; Batavia, Illinois; pp 1–63.

Saint-Gobain. Scintillating Optical Fibers. Saint-Gobain: Courbevoie, France 2005, pp 1–6.

CHAPTER 5

CONCLUSION

The purpose of this thesis was to design and optimize a miniaturized muon detector that is capable of being deployed in boreholes up to approximately 2 km underground. It requires the detector to be constrained in size to fit in about an 8 in. (approximately 20 cm) diameter pipe. Most muon detectors have areas in square meters, whereas the borehole deployment constrains the area to about 0.15 m^2 maximum. At the depths of interest, the muon flux drops rapidly, requiring the detector to make the most of the cosmic muons that reach it, which means a high efficiency is needed. Additionally, the detector must be robust in withstanding the pressure and caustic nature of some borehole fluids, requiring a thick encasing pipe to surround the detector. To resolve density changes in the rock formations above the detector with any usable accuracy, the detector will need to have an angular resolution sufficient to monitor changes to within a few meters. The simulations performed helped to develop and optimize the detector given these constraints. The preliminary experiments were used to understand the physical response of the scintillation materials used, the importance of using wavelength shifting fibers, and for basic validation of the simulation results.

One of the first challenges addressed was to quantify the muon flux at given depths. Previous research on this topic was insufficient because this research required a knowledge of how that flux changes with changes in CO_2 reservoir saturation. Two methods were devised of predicting flux changes based on reservoir depth and porosity, CO_2 saturation, and density of above-reservoir rock layers (overburden). The first method was based on a semiempirical equation for determining the muon energy and angular spectra at the surface of the earth. It was then modified in such a way that the muon energy represented a penetration depth into the earth.

This rendered the equation useful for predicting flux at depth, but did not account for density changes in the CO_2 storage reservoir. This equation was modified further by deriving an "equivalent depth" function that produces the depth "seen" by the detector as a function of physical depth, density, reservoir thickness, and CO_2 saturation and phase. Once this was done, an equation was completed that could predict the change in flux at any depth given the required parameters. The results of this calculation showed that the flux changes by approximately 1% for a 20% porosity reservoir that shifts in CO_2 saturation by 50%. To validate the derivation of the original flux at depth function derived, the second method was derived. To determine the muon flux at depth, an empirical equation for the muon flux at depth (with an error of about 0.5%) was modified by inserting the "effective depth" function previously derived. This made the existing empirical equation a function of physical depth, density, reservoir thickness, and CO_2 saturation and phase. These two methods showed comparable results, with an average deviation from each other of predicted muon flux of only 0.1%. The predicted flux changes due to CO_2 saturation are very small, less than 2%, and indicated the importance of developing a detector with very high accuracy. Meaning, when a muon event reaches the detector, it needs to be able to categorize it into the proper angle so that over a reasonable amount of time, the angular flux changes can be used to detect and locate shifts in the subsurface density from CO_2 injection or drifts. Thus, the angular resolution of the detector needs to be within a few degrees for statistical power.

It was shown through simulations that the 4-layer detector developed has a mean error of approximately 2 degrees using 1 cm scintillating rods. This low mean error will provide the necessary angular binning to detect changes in density in the reservoir above the detector. With a 30 meter reservoir and an average error of 2 degrees, the detector will locate a change in density in the center of the reservoir to within one meter. The most important insights gained from the simulations were the mean angular error (approximately 2 degrees) and the background discrimination capability of the detector. The mean angular error was determined by simulating the four-layer detector. The muon source for the main simulation was a full energy and angular spectra at sea level. The response of the detector was monitored by tracking the energy

deposited by each muon event. Each even was also monitored to see which type of particle was responsible for each energy deposit, with the secondary particle cut-off set at 1 keV. The amount of energy deposited in the rods of the same layer was used to determine the location chosen for the hit. Effectively, the energy deposit was used to average the bar location to give a more "pixelated" detector, so it isn't constrained to 1 cm segments in the coordinate axis. The simulations illuminated how the energy is shared between adjacent bars during hits, and from which particles. Bar sharing was significant and the simulations showed that spurious secondary particles can deposit energy in bars far away from the actual muon path. But, the simulation also showed that these events can be ignored in the postprocessing by using an averaging that only takes bars adjacent to the highest energy deposit. Knowledge of the way that energy is deposited and shared, gained by the simulations, allowed a successful background discrimination procedure to be developed. It was found that all of the gamma background radiation can be discriminated using four-fold coincidence and a simple energy threshold at approximately 200 KeV. Only gamma ray background was considered because alpha and beta particles were stopped by the encasing steel pipe. If any beta particles do make it through the steel pipe there is effectively no chance of them causing four-fold coincidence.

Because of how small the flux is at the deployment depths of interest (0.5 to 2 km), the detector must completely discriminate background events to take advantage of the very little muon data it will receive. In order to eliminate spurious events, radiation shielding was simulated by placing a metal shield between the inner two layers of the detector. It was shown that the use of shielding between the panels of the detector did nothing to improve the detector angular resolution. This was because the number of secondary particles absorbed by the shield were offset by the additional number of secondary particles produced by the shield.

The simulations provided the necessary physical insight to produce the working prototype; a four-layer scintillating detector inside of a steel pipe with coincidence and threshold electronics will perform all of the necessary functions needed for borehole deployment. Without the insights from the simulations, the detector construction and electronics would have been more difficult, more expensive due to multiple prototypes, the angular error would have been

impossible to determine prior to detector construction, and there would have been no way to prove the necessity of four-fold coincidence and an energy threshold.

The preliminary experiments were performed to explore the physical response of the scintillating rods, as well as the wavelength shifting fibers used. It was determined, through multiple experiments using radiation sources that the polystyrene scintillation bars have insufficient light transport. The wavelength shifting fibers were shown to be necessary to transport the light efficiently to the PMT. The experiments also showed that optical glue attaching the fiber to the inside of the bar is unnecessary for light transport efficiency, but adds mechanical stability. Further experiments were performed using coincidence electronics that were able to produce a sea-level muon spectrum. This spectrum was compared to the Geant4 simulations of the same double coincidence setup, and the results showed that the spectrum obtained by both experiment and simulation agreed. This gave validity the simulation predictions for the detector performance.

In conclusion, advanced Geant4 simulations and preliminary experiments have been performed to design and optimize the development of a miniaturized muon detector capable of being deployed in boreholes. The detector shows promise of being able to detect changes in the overburden thickness of subsurface reservoirs. The work contained in this thesis was performed primarily, if not entirely, by the author.